

# Magma ascent and degassing processes of the 2011 and 2017-18 eruptions of Shinmoedake in Kirishima volcano group, Japan, based on petrological characteristics and volatile content of magmas

Genji Saito (✉ [saitog@mac.com](mailto:saitog@mac.com))

Geological Survey of Japan, Advanced Industrial Science and Technology <https://orcid.org/0000-0002-7199-0692>

Teruki Oikawa

Geological Survey of Japan, Advanced Industrial Science and Technology

Osamu Ishizuka

Geological Survey of Japan, Advanced Industrial Science and Technology

---

## Research Article

**Keywords:** Kirishima volcano, Shinmoedake, Eruption, Petrology, Magma mixing, Magma ascent, Degassing, Melt inclusions, Volatile content, Bubble volume

**Posted Date:** March 24th, 2022

**DOI:** <https://doi.org/10.21203/rs.3.rs-1449052/v1>

**License:**  This work is licensed under a Creative Commons Attribution 4.0 International License.

[Read Full License](#)

---

**Version of Record:** A version of this preprint was published at Earth, Planets and Space on May 23rd, 2023. See the published version at <https://doi.org/10.1186/s40623-023-01836-1>.

# Abstract

The eruption activity of Shinmoedake in the Kirishima volcanic group of Japan resumed in 2017–18 after a quiet period that lasted between 2011 and 2017. Subplinian eruptions preceded lava effusion in 2011; however, no subplinian eruption occurred in 2017–18. Petrological studies and melt inclusion analyses were conducted to investigate the ascent and degassing of the magma to understand the cause of the different eruption styles. Chemical analysis of the melt inclusions from the 2011 eruption indicates that mafic magma with high volatile content (6.2 wt% H<sub>2</sub>O, 1.4–0.25 wt% CO<sub>2</sub>) ascended into the shallow felsic magma (3.7–1.9 wt% H<sub>2</sub>O, 0.048–0.025 wt% CO<sub>2</sub>) at depths of 4–5 km. Calculations indicate that the mafic magmas were of lower density (1717–1835 kg m<sup>-3</sup>) than the felsic magma (2264–2496 kg m<sup>-3</sup>) at 125 MPa and that the two magmas were mixed. The 2011 mixed magma with high volatile content (4.0 wt% H<sub>2</sub>O, 0.14–0.70 wt% CO<sub>2</sub>) had a bubble volume of approximately 50 vol% at 50 MPa, which is likely to have caused the subplinian eruption. The whole-rock and chemical compositions of the plagioclase-, clinopyroxene-, and orthopyroxene phenocryst cores were similar in 2018 and 2011, suggesting that the 2018 magma was a remnant of the 2011 magma. Chemical analyses of the groundmass from 2018 and the MELTS calculation indicate that the magma approached chemical equilibrium over the period 2011 to 2018. Melt inclusion analyses and volcanic gas observation gave a lower bulk volatile content for the 2018 magma (3.0–2.1 wt% H<sub>2</sub>O, 0.10–0.087 wt% CO<sub>2</sub>) compared to the 2011 magma. Comparison of the degassed-magma volumes estimated from the S and Cl contents of the melt inclusions, SO<sub>2</sub> flux and volcanic gas composition, and erupted-magma volume indicates that excess degassing has been occurring in the magma due to convection since March 2011, which may have decreased the volatile content of the magma. The relatively low volatile content meant that the 2018 magma could not erupt explosively and lava was instead erupted via effusion.

## Introduction

The behavior of volatiles in magma chambers is a highly important factor that both influences and controls eruptions. A vapor phase of more than 5 vol% that accumulated in the magma chamber of Mt. Pinatubo by 1991 may have been associated with the Plinian eruption that occurred shortly afterward (Gerlach et al. 1996). However, the effective degassing of magma in the chamber of an approximately 1 km<sup>3</sup> dacitic-lava dome at Mt. Unzen in 1991–95 resulted in an effusive eruption (Ohba et al. 2008). These results indicate that eruption styles depend on the volatile content and degassing processes of a magma chamber. It is therefore important that the volatile behavior and degassing processes of magmas are studied in order to better understand the mechanisms surrounding volcanic eruption. Petrological studies investigating volcanic rocks allow elucidation of the physical and chemical conditions of a magma chamber, including factors such as temperature, chemical composition, and the properties of an end-member magma if mixing occurred. Melt-inclusion analysis is a powerful method for estimating the volatile content of the melt in a magma prior to eruption [e.g., Anderson 1973; Anderson et al. 1989; Johnson et al. 1994; Lowenstern 2003]. Because melt inclusions preserve the chemical compositions of a melt at the time of phenocryst growth, the volatile content of the melt in each end-member magma

resulting from the magma-mixing process can be estimated. Moreover, combining melt-inclusion analysis with volcanic gas observation can be used to estimate the volume of a degassed magma.

This study is an investigation of the magma ascent and degassing processes during a series of eruptions from 2011–18 at Shinmoedake in the Kirishima volcanic group. The 2011 eruptions were marked by a series of phreatomagmatic- and subplinian eruptions followed by vulcanian explosions and the effusion of lava within the summit crater (Nakada et al. 2013). Continuous degassing activity with intermittent vulcanian explosions and continuous ash emissions were also observed from January to September 2012 (Mori and Kato 2013). The 2017–18 eruptions involved vulcanian explosions and lava effusion in the summit crater during March 2018 that were followed by small ash eruptions in October 2017; however, no subplinian eruptions occurred. Such differences provide a useful opportunity for us to investigate the relationship between eruption style and the physical and chemical conditions of a magma. Petrological studies and melt-inclusion analyses of the Shinmoedake eruptions were therefore conducted to understand the physical and chemical conditions in the magma chambers and the amount of degassed magma present during the different active periods. Geological, geophysical, and geochemical observations were thus combined to model the magma ascent and degassing processes during the 2011 and 2017–18 Shinmoedake eruptions.

## **Overview Of The Kirishima Volcano Group And The 2011 And 2017–18 Shinmoedake Eruptions**

The Kirishima volcanic group is located in southern Kyushu, Japan (Figure. 1). The group extends over an area of about 20 × 30 km and contains more than 20 small volcanoes (Imura and Kobayashi 2001). Historically, the group can be divided into older and younger volcanoes; activity started in the older volcanoes at around 1.2 Ma and continued until several hundred thousand years ago, while the younger volcanoes first became active around 300 ka with activity continuing to the present time. The composition of the rocks in the younger Kirishima volcanoes ranges from olivine basalt to pyroxene andesite and hornblende-bearing pyroxene dacite. Shinmoedake, one of the younger volcanoes, first became active at approximately 18 ka. Since 742, all eruptions have occurred at the Shinmoedake and Ohachi volcanoes in the southeastern part of the Kirishima volcanic group, except for Ioyama (Figure. 1). The eruptions at Ohachi in 788 and 1235 and Shinmoedake over the period 1716–17 were explosive and ejected pyroclastic flows that caused significant disasters. Some minor and phreatic eruptions also occurred at Shinmoedake in 1959, 1991, and 2008 (Geshi et al. 2010).

The 2011 series of Shinmoedake eruptions started with phreatomagmatic eruptions on 19 January 2011 (Kato and Yamasato 2013; Miyabuchi et al. 2013; Nakada et al. 2013). Three subplinian eruptions during the period 26–27 January (the “P1, P2, and P3 events”) produced a total tephra mass of  $1.7\text{--}2.8 \times 10^{10}$  kg (Maeno et al., 2014). These eruptions were followed by lava effusion within the summit crater (28 January to 1 February) and vulcanian explosions. A dense-rock equivalent (DRE) of approximately  $15 \times 10^6$  m<sup>3</sup> of effused lava was produced (Kozono et al. 2013; Nakada et al. 2013). Observations of the

volcano by the Global Positioning System (GPS) indicated that it was undergoing continuous inflation from December 2009 (Kawamoto et al. 2011), while significant deflation by approximately  $14 \times 10^6 \text{ m}^3$  was observed as a result of the subplinian eruptions and lava effusion (Imakiire and Nishimura 2012; Nakao et al. 2013). Vulcanian explosions and continuous ash emissions from the summit crater occurred intermittently from February–September (Nakada et al. 2013), and an estimated  $4.2 \times 10^8 \text{ kg}$  of tephra was erupted during seven events from 24 February to 7 September (Nishiki et al. 2013). Petrological study of ash samples from the eruptions during March–June indicated that more than half of the volume of the ash was composed of essential material (Oishi et al. 2013; Suzuki et al. 2013a). GPS observation indicated that inflation restarted on 2 February and continued until November 2011, at which point it ceased (Imakiire and Nishimura 2012; Nakao et al. 2013). The intense gas emission that started with the eruptive activity peaked at  $490 \text{ kg s}^{-1} \text{ SO}_2$  ( $42600 \text{ t d}^{-1} \text{ SO}_2$ ) on 28 January (Mori and Kato 2013), after which it gradually decreased to reach approximately  $1 \text{ kg s}^{-1} \text{ SO}_2$  by the end of 2011 (Mori and Kato 2013).

The activity then resumed with small eruptions of ash on 11–16 October 2017 after a rest period of approximately 6 y. A small ash eruption that started on 1 March 2018 rapidly changed to ash eruptions with vulcanian explosions and lava effusion within the summit crater on 6 March 2018. The lava effusion continued until 9 March, and the vulcanian explosions and ash eruptions continued intermittently until 27 June 2018. One difference in the eruption styles observed in 2011 and the 2017–18 is that subplinian eruptions did not occur in 2017–18. Approximately  $15 \times 10^6 \text{ m}^3$  Dense-Rock Equivalent (DRE) of effused lava was produced during this period (Chiba et al. 2018; Oikawa et al. 2018). Continuous inflation of the volcano observed from 1 July 2017 to 1 March 2018 (JMA, 2019) was followed by deflation of approximately  $7 \times 10^6 \text{ m}^3$  (JMA, 2019b) during the vulcanian eruptions and the lava effusion of 1–10 March 2018. The inflation then restarted and continued until 31 January 2019. The intense gas emission that started in October 2017 and peaked at  $390 \text{ kg s}^{-1} \text{ SO}_2$  ( $34000 \text{ t d}^{-1} \text{ SO}_2$ ) on 7 March 2018 (JMA, 2019) decreased gradually to reach approximately  $1 \text{ kg s}^{-1}$  by October 2018 (JMA, 2019).

## Sampling And Analytical Methods

### Samples

Eruptive products that were analyzed from the 1716–17 and 2011 eruptions of Shinmoedake volcano (Table 1) include gray and white colored pumices from the 1716–17 eruption (hereafter “1716–17GP” and “1716–17WP”; Table 1), pumices from the phreatomagmatic eruption on 19 January 2011 (hereafter “2011–1PP”), gray and white pumices from the subplinian eruptions during events P2 and P3 on 26–27 January 2011 (hereafter “2011–2SGP and 2011–2SWP” for event P2 and “2011–3SGP” for event P3), and a bomb and lapillus from the vulcanian explosions of February 2011 (“2011–4VB” and “2011–5VL”). Although both gray and white pumices were ejected during the 2011 subplinian eruptions (Suzuki et al. 2013b; Tomiya et al. 2013), the majority was gray. Ash particles and lapilli from the vulcanian and ash

eruptions during March–August 2011 were also examined in this study (“2011–6VA”, “2011–7VL”, “2011–8A”, and “2011–9A”; Table 1) along with eruptive products from the 2018 eruptions (Table 1); gray colored pumices and scoria from the vulcanian explosion on 6 and 9 March 2018 (hereafter “2018–1VGP” and “2018–1VS” for the 6 March products and “2018–2VGP” and “2018–2VS” for the 9 March products; Table 1), three ballistic blocks from the vulcanian eruptions (“2018–3BB1, BB2, and BB3”), two dark-gray and lithic lava fragments (“2018–4L1 and L2”), a gray and porous lava fragment (“2018-4L3”), and a banded and porous lava fragment (“2018-4L4, L5”). Scoria from the 1235 eruption of Ohachi volcano was also analyzed (“1235S” in Table 1). Detailed descriptions of the samples are summarized in Table 1 and their sampling locations are noted in Fig. 1.

## Analytical methods

The major-element compositions of the 1235S, 2011-7VL, and 2018 eruptive products were determined using wavelength-dispersive X-ray fluorescence analysis (XRF; Table 2; Ishizuka et al. 2014). Glass beads, prepared by fusing 1:10 mixtures of 0.5 g subsamples and lithium tetraborate, were analyzed using a Panalytical Axios XRF spectrometer at the Geological Survey of Japan (GSJ), AIST (Advanced Industrial Science and Technology). The pumices, scoria, bomb, lapilli, ashes, and lava fragments from the 2011 and 2018 eruptions were mounted in epoxy resin, ground with sandpaper, and then polished with diamond powder (1  $\mu\text{m}$ ). The mode compositions and porosities of the samples were determined using backscattered electron (BSE) images by scanning electron microscopy (SEM; Additional file 1). Chemical analyses of the phenocrysts, melt-inclusions, groundmass microlites (< 0.1 mm), and the bulk composition of the groundmass were carried out using electron probe micro-analyzers (EPMA; JEOL JXA-8900 and JEOL JXA-8530F at GSJ, AIST). The experimental conditions used for the analysis of minerals and groundmass were identical to those reported by Saito et al. (2002) and Saito et al. (2001). Compositional profiles across the olivine, plagioclase, and pyroxene phenocrysts from core to rim were also determined by EPMA. The major-element contents and the minor S and Cl contents of the melt inclusions were determined by EPMA, with an accelerating voltage of 15 keV, a beam current of 10 nA, and a defocused beam with a diameter of 5  $\mu\text{m}$  (Table 3). The S K $\alpha$  radiation wavelength was used for S analysis to determine the sulfide and sulfate proportions in the inclusions (Wallace and Carmichael 1994). The H<sub>2</sub>O content of the inclusions was estimated by EPMA, for which it was assumed that the H<sub>2</sub>O content was equal to the difference between 100% and the sum of the other measured contents. The error of  $\pm 1$  wt% that was used for this estimation is based on repeated analyses of standard glass samples (Saito et al., 2018).

The H<sub>2</sub>O and CO<sub>2</sub> contents of the melt inclusions in the eruptive products from 1235, 1716-17, 2011, and 2018 were measured by secondary ion mass spectrometry (SIMS) (Tables 1 and 3). The mounted samples were polished with Al<sub>2</sub>O<sub>3</sub> powder (1  $\mu\text{m}$ ) and coated with gold prior to the SIMS analyses with a Cameca ims-1270 SIMS (installed at GSJ, AIST). A detailed description of the SIMS analyses performed can be found in Saito et al. (2010) and Saito et al. (2018). A Cameca nanoSIMS 50L (installed at GSJ, AIST) was used to measure the H<sub>2</sub>O and CO<sub>2</sub> contents in the melt inclusions from the 2018 eruptions. In

both analyses, Cs<sup>+</sup> ions were used as the primary beam and negatively charged secondary <sup>1</sup>H, <sup>12</sup>C, and <sup>30</sup>Si ions were collected (Hauri et al. 2002). A limited area measuring 10 × 10 μm on the sample surface was analyzed to avoid the crater-edge effect (Saito et al. 2010). A normal-incidence electron gun was used for charge compensation of the sample based on the methods by Kita et al. (2004). SIMS calibration lines were made for H<sub>2</sub>O and CO<sub>2</sub> on each measurement day using the reference glasses. Repeated analyses of the same melt inclusions indicated an analytical error of not more than ± 0.2 wt % for H<sub>2</sub>O and ± 0.0028 wt % for CO<sub>2</sub> (Saito et al., 2010).

## Results

### Whole-rock and mode compositions

The products of the 2011 eruptions (2011-2SGP, 2011-3SGP, 2011-4VB, 2011-5VL and 2011-7VL) were found to have andesite composition (SiO<sub>2</sub> = 57–58 wt.%), which is similar to that of 1716-17GP (Table 2; Fig. 2). 2011-2SWP has a dacite composition (SiO<sub>2</sub> = 63 wt.%), which is similar to 1716-17WP. Suzuki et al. (2013b) concluded that most of the ejecta from the 2011 eruptions are mixed magma products (SiO<sub>2</sub> = 57–58 wt.%, 960–980 °C) of felsic magma (silicic andesite having SiO<sub>2</sub> = 62–63 wt.% and 870 °C) and mafic magma (basaltic andesite having SiO<sub>2</sub> = 55 wt.% and 1030 °C). The products of the 2011 eruptions (2011-2SGP, 2011-3SGP, 2011-4VB, 2011-5VL, and 2011-7VL) with andesite composition are therefore mixed products and 2011-2SWP, with a dacite composition, was derived from the silicic andesite magma chamber.

The products of the 2018 eruptions have SiO<sub>2</sub> content of 58–59 wt.% and K<sub>2</sub>O content of 1.6–1.7 wt.%, which is similar or a little more evolved than 2011-2SGP and 2011-3SGP. However, the porous gray lava samples from the 2018 eruptions (2018-4L3 and 2018-4L5) (Table 2; Fig. 2) have similar chemical compositions to 2011-2SWP. This result indicates that two different magmas that were similar to those from 2011 and 1716–17 were erupted in 2018; one an andesitic magma with SiO<sub>2</sub> = 57–59 wt.% and K<sub>2</sub>O = 1.5–1.7 wt% and the other dacite with SiO<sub>2</sub> = 63 wt.% and K<sub>2</sub>O = 2.4–2.5 wt%. This suggests that the same magma system was present in 1716–17 and 2018. On the other hand, the major-element composition of 1235S is basaltic andesite and is similar to lava from the 7 ka eruption at Takachihonomine (Table 2). 2011-2SGP and 2011-3SGP are composed of 20–21 vol% plagioclase phenocrysts, 1–2 vol% clinopyroxene- and orthopyroxene phenocrysts, < 1 vol% olivine phenocrysts, < 1 vol% Fe-Ti oxides, and 72–74 vol% groundmass (Additional file 1). 2011-2SWP has a mode composition similar to the subplinian gray pumice. 2011-4VB, 2011-5VL, 2011-6VA, and 2011-7VL also have mode compositions that are similar to those of the subplinian gray pumices from January 2011, but their groundmass contents (66–71 vol%) are slightly lower. The porosities of products from the subplinian eruptions (42–54 vol% of 2011 levels at -2 to -4) are a little higher than those of the vulcanian bomb, ash, and lapilli (2–40 vol% of 2011 levels at -4 to -7; Additional file 1). 2018-1VGP and 2018-2VGP are composed of 20–22 vol% plagioclase phenocrysts, 8 vol% clinopyroxene and orthopyroxene phenocrysts, < 1 vol% Fe-Ti oxides, and 70–72 vol% groundmass (Additional file 1). 2018-1VS and 2018-2VS have

slightly less plagioclase (16–17 vol%) and a slightly higher pyroxene content (11 vol% clinopyroxene and orthopyroxene phenocrysts) than the vulcanian gray pumices, although they have similar groundmass contents (72–73 vol%). The groundmass contents of 2018-4L1, 2018-4L2 (67–69 vol%), and 2018-4L3 (54 vol%) are lower than those of the vulcanian gray pumices and scoria. 2018-4L3 has the highest phenocryst content of 46 vol% (and the lowest groundmass content of 54 vol%). Considering its andesite composition ( $\text{SiO}_2 = 62.65$  wt.%; Table 2), it is likely a silicic andesite end member ( $\text{SiO}_2 = 62\text{--}63$  wt% and 43 vol% phenocryst content) estimated by Suzuki et al. (2013b). The pumices, scoria, and lava from the 2018 eruptives contain no olivine phenocrysts, except for 2018-2VS with olivine phenocrysts of less than 1 vol% (Additional file 1). The rare olivine phenocrysts in 2018-2VS have a reaction rim composed of orthopyroxene (Additional file 2I). These observations suggest that olivine could not stabilize in the 2018 magma chamber.

## Chemical compositions of minerals and groundmasses

The cores of the plagioclase phenocrysts (hereafter “plagioclase-phenocryst cores”) in the 2011 eruption products have variable composition ( $\text{An}_{42-94}$ ) with major  $\text{An}_{84-94}$  and  $\text{An}_{50-62}$  populations (Fig. 3a). The two populations indicate that mafic magma has been mixed with high-An plagioclases, and felsic magma with low-An plagioclases. Significant variation was also observed in the rims of the plagioclase-phenocrysts (hereafter “plagioclase-phenocryst rims”) with two peaks at around  $\text{An}_{50-60}$  and  $\text{An}_{66-76}$  (Fig. 3b). In contrast, the plagioclase cores (< 0.1 mm) in the groundmass (hereafter “groundmass-plagioclase cores”) show variation of  $\text{An}_{40-90}$  with only one peak observed (Fig. 3c). The small variation indicates that the groundmass is a mixed product. In comparison, the significant variation observed in the plagioclase-phenocryst rims suggests that the plagioclase phenocrysts did not regrow after mixing, implying that the eruption occurred soon after mixing occurred. Similar variations are observed in the plagioclase-phenocryst cores ( $\text{An}_{44-91}$ ) and rims ( $\text{An}_{50-90}$ ), and in the groundmass-plagioclase cores ( $\text{An}_{57-88}$ ) of the 2018 products (Fig. 3a-c). This similarity indicates that the magmas that were erupted in 2011 and 2018 formed via mixing of the same end-member magmas. Of the 222 plagioclase phenocrysts from 2011, 10% (2011-1PP to 2011-7VL) have rims reaching more than 0.1 mm in length (Additional file 2), while 28% of the 85 plagioclase phenocrysts in the 2018 products have such wide rims. The increase in the fraction of plagioclases with wide rims suggests that the magma chamber was able to crystallize over this period. Clinopyroxene-phenocrysts from the 2011 products have cores of  $\text{Wo}_{34-45}\text{En}_{40-47}\text{Fs}_{13-20}$  and  $\text{Mg}\#70\text{--}77$  (Fig. 3g), and rims of  $\text{Wo}_{33-45}\text{En}_{40-50}\text{Fs}_{13-19}$  and  $\text{Mg}\#70\text{--}80$  (Fig. 3h), while the groundmass-clinopyroxene cores show  $\text{Wo}_{15-44}\text{En}_{34-62}\text{Fs}_{13-36}$  and significant variation in  $\text{Mg}\#$  ( $\text{Mg}\#60\text{--}76$ ) (Fig. 3i). Similar variations are observed in the clinopyroxenes from the 2018 eruptions (phenocryst cores of  $\text{Wo}_{39-46}\text{En}_{38-45}\text{Fs}_{14-18}$  and  $\text{Mg}\# 69\text{--}76$ , phenocryst rims of  $\text{Wo}_{38-46}\text{En}_{37-46}\text{Fs}_{14-18}$  and  $\text{Mg}\# 68\text{--}76$ , and groundmass-clinopyroxene cores of  $\text{Wo}_{12-43}\text{En}_{40-64}\text{Fs}_{12-28}$  and  $\text{Mg}\# 67\text{--}79$ ; Fig. 3g-i). The similar chemical composition of the clinopyroxene-phenocryst cores from 2011 and 2018 indicates that these clinopyroxenes were from the same source.

The orthopyroxene-phenocrysts in the 2011 products have cores of  $Wo_{1-6}En_{61-77}Fs_{21-36}$  and Mg#63–79, and rims of  $Wo_{2-5}En_{62-74}Fs_{23-38}$  and Mg#62–76 (Fig. 3j-k), with the groundmass-orthopyroxene cores showing similar composition ( $Wo_{2-11}En_{57-74}Fs_{22-35}$  and Mg# 60–76), (Fig. 4l). The Mg# is bimodally distributed in the orthopyroxene-phenocryst rims (Mg#64–68 and Mg#72–74; Fig. 3e). Most of the groundmass-orthopyroxene cores show a peak at Mg#70–74. The high-Mg# orthopyroxene-phenocryst rims therefore appear to have grown simultaneously with the formation of the groundmass-orthopyroxene cores. The low-Mg# rims on some of the orthopyroxene phenocrysts indicates that the period between mixing and eruption was too short to allow high-Mg# rims to grow on all phenocrysts. Orthopyroxene phenocrysts from the 2018 eruptions have cores of  $Wo_{2-4}En_{61-75}Fs_{22-37}$  and Mg# 62–77 and rims of  $Wo_{2-5}En_{61-74}Fs_{23-36}$  and Mg# 63–77 with groundmass-orthopyroxene cores of  $Wo_{2-8}En_{63-76}Fs_{20-34}$  and Mg# 65–79 (Fig. 3j-k). The orthopyroxene-phenocryst cores show bimodal Mg# distribution, similar to those in the 2011 products (Fig. 3j), indicating that the magmas that were erupted in 2011 and 2018 formed by mixing of the same end-member magmas. Although the orthopyroxene-phenocryst rims have bimodal Mg# distribution in the same manner as the 2011 samples (Mg#64–68 and Mg#72–74; Fig. 4e), more high-Mg# (Mg#72–74) orthopyroxene-phenocryst rims formed as compared to 2011. This discrepancy suggests that the high-Mg# orthopyroxene-phenocryst rims from the 2018 samples were able to grow in the magma chamber over the period 2011–2018.

All clinopyroxene phenocrysts in the 2011 products observed in this study have rims of less than 0.05 mm (Additional file 2). On the other hand, 13% of the 68 clinopyroxene phenocrysts from 2018 have rims reaching more than 0.05 mm in length, and the maximum width of the clinopyroxene-phenocryst rims from the 2018 eruptions is 0.16 mm. The fraction of orthopyroxene phenocryst with rims larger than 0.05 mm increased from 3% in 2011 (130) to 21% in 2018 (82). The maximum width of the orthopyroxene-phenocryst rims also increased from 0.07 mm in 2011 to 0.16 mm in 2018. The increases in the numbers of clinopyroxenes and orthopyroxenes with wide rims and the maximum width of the rims from 2011 to 2018 suggest that the magma chamber crystallized over time, as did the plagioclase-phenocryst rims.

The olivine phenocrysts in the 2011 products have core compositions of  $Fo_{74-80}$  (Fig. 3d). The olivine-phenocryst rims and groundmass-olivine cores from 2011 vary more ( $Fo_{60-76}$  and  $Fo_{52-78}$ , respectively) than the olivine-phenocryst cores in terms of composition (Fig. 3e and 3f). The olivine phenocrysts have rims that show normal zoning with widths of less than 0.06 mm (Additional file 2), while olivine phenocrysts are rarely observed in the 2018 products (Additional file 1) and the phenocrysts that are present (2) have large orthopyroxene rims (Additional file 2l). No groundmass-olivines were found in the 2018 products. These observations indicate that the physical and chemical conditions during the formation of the 2018 magma were not stable enough for olivines to form.

The groundmasses of the eruption products from January 2011 (2011-1PP, 2011-2SGP, and 2011-3SGP) have andesite compositions: 61–62 wt%  $SiO_2$ , and 2.1–2.2 wt%  $K_2O$  (normalized to volatile-free basis; Additional file 3; Fig. 4), except for 2011-2SWP, which has a rhyolitic composition (71 wt%  $SiO_2$ , and 3.8 wt%  $K_2O$ ; Additional file 3; Fig. 4). The groundmasses of the products from February 2011 (2011-4VB and

2011-5VL) have slightly SiO<sub>2</sub>- and K<sub>2</sub>O-rich compositions (63–64 wt% SiO<sub>2</sub> and 2.4 wt% K<sub>2</sub>O) compared to the subplinian gray pumices. The groundmasses in the eruption products from March–August 2011 (2011-6VA to 2011-9A) have richer SiO<sub>2</sub> and K<sub>2</sub>O compositions (62–65 wt% SiO<sub>2</sub> and 2.0–2.8 wt% K<sub>2</sub>O), except 2011-8A (GG-type). The groundmass of 2011-8A (GG-type) has a highly evolved composition (68 wt% SiO<sub>2</sub> and 3.5 wt% K<sub>2</sub>O), which is similar to that of 2011-2SWP. These results indicate that the melt in the magma chamber gradually transformed to a high-SiO<sub>2</sub> and -K<sub>2</sub>O composition between January and August 2011. The groundmasses of 2018-1VGP, 2018-1VS, 2018-2VGP, 2018-2VS, and 2018-4 L1 and L2 (dark-gray and lithic lava) have a dacite composition: 64–66 wt% SiO<sub>2</sub>, and 2.5–2.9 wt% K<sub>2</sub>O (Additional file 5; Fig. 4). These compositions are similar to or a little evolved compared to the eruptive products from March–August 2011. This similarity suggests that the melt in the 2018 magma was a remnant of the melt in the 2011 magma. On the other hand, the groundmass of 2018-4L3 (gray and porous lava) has a rhyolite composition (75 wt% SiO<sub>2</sub>, and 4.5 wt% K<sub>2</sub>O; Additional file 3; Fig. 4), which is the highest SiO<sub>2</sub> and K<sub>2</sub>O contents among the groundmasses observed in the 2011–2018 products.

## Melt inclusions

Four melt inclusions from 1235S, 16 inclusions from 1716-17GP, 79 inclusions in the 2011 eruptive products (2011-1PP to 2011-7VL), and 24 inclusions from 2018-1VGP were analyzed in this study (Table 1; Table 3; Additional file 4). Most inclusions are glassy, but several contain minerals and/or bubbles, and are found in the olivine, clinopyroxene, orthopyroxene, plagioclase, and ilmenite phenocrysts (Table 3; Additional file 4). Most inclusions are elliptical or quadrilateral in shape and range from 0.01 to 0.15 mm in diameter (Fig. 5). BSE images of the melt inclusions in the olivines show overgrowth of 1–2 μm. The chemical compositions of these inclusions were corrected for post-entrapment crystallization by adding the host-olivine component until an olivine-melt equilibrium was reached, assuming that  $K_D = 0.30$  (Roedder and Emslie 1970; Saito et al. 2010). Olivine overgrowth of 0–5.3 wt% was estimated via this method (Table 3; Additional file 4).

One inclusion found in an olivine from 1235S has andesite composition (59 wt% SiO<sub>2</sub> and 1 wt% K<sub>2</sub>O) while three inclusions in the clinopyroxenes from 1235S have dacite composition (63–68 wt% SiO<sub>2</sub> and 1–2 wt% K<sub>2</sub>O) (Table 3; Fig. 6). Sixteen inclusions in 1716-17GP have dacite to rhyolite compositions (62–76 wt% SiO<sub>2</sub> and 2–5 wt% K<sub>2</sub>O; Table 3; Fig. 6; Additional file 4). Inclusions from the 2011 eruptions can be divided into two types: andesite inclusions in olivine phenocrysts (34 inclusions) with 53–62 wt% SiO<sub>2</sub> and 1–3 wt% K<sub>2</sub>O, and dacite-rhyolite inclusions in the plagioclase, clinopyroxene, and orthopyroxene phenocrysts (8 inclusions with 72–75 wt% SiO<sub>2</sub> and 4–5 wt% K<sub>2</sub>O in the plagioclase phenocrysts, 18 inclusions with 68–76 wt% SiO<sub>2</sub> and 3–7 wt% K<sub>2</sub>O in the clinopyroxene phenocrysts, and 17 inclusions with 68–78 wt% SiO<sub>2</sub> and 3–5 wt% K<sub>2</sub>O in the orthopyroxene phenocrysts). The inclusions from the 2018 eruptions have andesite to rhyolite compositions; 6 inclusions in the plagioclase phenocrysts have 72–73 wt% SiO<sub>2</sub> and 4 wt% K<sub>2</sub>O, 6 inclusions in the clinopyroxene phenocrysts have 71–76 wt% SiO<sub>2</sub> and 4–5 wt% K<sub>2</sub>O, and 12 inclusions in the orthopyroxene phenocrysts have 60–75 wt% SiO<sub>2</sub> and 2–4 wt% K<sub>2</sub>O. The chemical composition of the andesite and rhyolite inclusions did not differ

greatly (Fig. 4). Less-evolved chemical compositions of < 60 wt% SiO<sub>2</sub> and < 2 wt% K<sub>2</sub>O in the 2011 samples were not observed in the inclusions from 2018, which have intermediate compositions rather than the andesite and dacite-rhyolite inclusions observed in the 2011 eruptives.

Significant variation is observed in the H<sub>2</sub>O, CO<sub>2</sub>, and S contents of the andesite inclusions within the olivine phenocrysts, which range from 1.4 to 7.0 wt% for H<sub>2</sub>O (by SIMS), from 0.001 to 0.054 wt% for CO<sub>2</sub>, and from 0.019 to 0.170 wt% S (Fig. 8; Table 3; Additional file 4). These large variations are uncorrelated with the SiO<sub>2</sub> and K<sub>2</sub>O contents of the inclusions, indicating that the differences were not the result of fractional crystallization. Furthermore, inclusions with high H<sub>2</sub>O content (> 4 wt%) have high S content (0.148–0.170 wt%; Fig. 8; Table 3). These results indicate that the observed variation may have been caused by the exsolution of H<sub>2</sub>O and S from the andesite melt. On the other hand, relatively small variation was observed in the Cl content of the inclusions (0.053–0.092 wt%), except for 2 inclusions in 11-4V-p8i1 and 11-1P-p11i that have high Cl contents (0.165 wt% and 0.121 wt%, respectively). These high Cl content inclusions are accompanied by high SiO<sub>2</sub> and K<sub>2</sub>O contents (61.80 wt% SiO<sub>2</sub> and 2.91 wt% K<sub>2</sub>O and 61.16 wt% SiO<sub>2</sub> and 2.84 wt% K<sub>2</sub>O, respectively), suggesting that the increase in the Cl contents was due to crystallization.

Large variation is also observed in the H<sub>2</sub>O, CO<sub>2</sub>, and Cl contents of the dacite-rhyolite inclusions from the 2011 eruptions, which range from 1.4 to 4.8 wt% for H<sub>2</sub>O (by SIMS), 0.002 to 0.048 wt% for CO<sub>2</sub>, and 0.040 to 0.166 wt% for Cl (Fig. 8; Table 3; Additional file 4). These large variations are uncorrelated with the SiO<sub>2</sub> and K<sub>2</sub>O contents in the same inclusions, indicating that the differences were not caused by fractional crystallization but were rather the result of degassing in the dacite-rhyolite melt. Most of the inclusions have S contents of less than 0.02 wt%, although four of the samples: 11-1P-p7i1, 11-4V-p6i1, 11-4V-p7i1, and 11-4V-p12i1 have inclusion S contents of 0.034–0.061 wt% S. These inclusions with relatively high S contents and low SiO<sub>2</sub> contents (67.85–70.35 wt%; Table 3; Additional file 4) suggest that the high S contents were the result of mixing high S content mafic melt with rhyolite melt.

The andesite-rhyolite inclusions in the 2018 eruptions also show large variations in terms of H<sub>2</sub>O, S and Cl contents, which range from 0.5 to 5.0 wt% for H<sub>2</sub>O (by SIMS), 0.003 to 0.138 wt% for S, and 0.065 to 0.166 wt% for Cl (Fig. 7; Table 3; Additional file 4). The CO<sub>2</sub> contents in these inclusions are less than 0.027 wt%. The maximum H<sub>2</sub>O, CO<sub>2</sub>, and S contents in the andesite inclusions from the 2018 eruptions (5.0 wt% H<sub>2</sub>O, 0.021 wt% CO<sub>2</sub>, and 0.138 wt% S) are lower than those in the andesite inclusions from the 2011 eruptions (7.0 wt% H<sub>2</sub>O, 0.054 wt% CO<sub>2</sub>, and 0.0170 wt% S) (Fig. 7; Table 3; Additional file 4), suggesting that the andesite melt in the 2018 magma was volatile-poor compared to the 2011 magma. The large variations in the H<sub>2</sub>O, S, and Cl contents of the andesite-rhyolite inclusions from 2018 are roughly correlated with the SiO<sub>2</sub> contents of the inclusions; those with lower SiO<sub>2</sub> content have higher H<sub>2</sub>O, S, and Cl contents (Fig. 7). The results indicate that these variations were likely caused when mafic melt with high H<sub>2</sub>O, S, and Cl contents mixed with felsic melt of low H<sub>2</sub>O, S, and Cl contents.

# Physical And Chemical Conditions In The Magma From 2011–18

## Temperature of the magma

Two-pyroxene thermometry (Putirka 2008) was applied to the compositions of the borders of intergrown clinopyroxene and orthopyroxene phenocrysts from the 1716–17, 2011, and 2018 eruptions. A temperature of 948 °C was obtained for the intergrown phenocrysts from the 1716–17 eruptions and the intergrown phenocrysts from all eruptions in 2011 (2011-1 PP to 2011-9A) gave similar temperatures (908–945 °C; Additional file 5), except 2011-8A, for which the intergrown phenocryst yielded a higher temperature estimate ( $1055 \pm 10$  °C). 2011-2SWP, with a dacite whole-rock composition (Table 2), showed the lowest temperature of 908 °C in the 2011 eruptives. Two-pyroxene thermometry indicated that the temperature of the 2018 eruptives (914–944 °C) are similar to those of the 2011 eruptives. 2018-4L3, with a whole-rock dacite composition, showed the lowest temperature of the 2018 eruptives at 914 °C, which is similar to the temperature of 2011-2SWP (908 °C) with dacite composition.

FeTi oxide thermometry (Anderson et al. 1993) was also applied to the border compositions of intergrown magnetite and ilmenite phenocrysts from the 1716–17, 2011, and 2018 eruptions (Additional files 5 and 6). The compositions of the intergrown phenocrysts in 1716-17GP gave a temperature of 940 °C (Additional file 5) and an oxygen fugacity ( $\log f_{O_2}$ ) of -9.9 log units (2.0 log units above the FMQ buffer; Additional file 6), while the compositions of the intergrown phenocrysts from the 2011 eruptions (2011-1 PP to 2011-5VL) gave temperatures of 891–977 °C (Additional file 5) and oxygen fugacities ( $\log f_{O_2}$ ) of -12.1 to -9.7 log units (0.6–1.3 log units above the FMQ buffer; Additional file 6). The temperature estimated for the 2011 magma by FeTi oxide thermometry is similar to that obtained by two-pyroxene thermometry, except for the slightly higher temperature obtained for 2011-4VB (977 °C) by FeTi oxide thermometry. In addition, the temperatures of 2018-1VGP, 2018-1VS, 2018-2VGP, 2018-2S, 2018-4L1, and 2018-4L2 (944–985 °C) estimated by FeTi oxide thermometry are similar to those obtained by two-pyroxene thermometry (914–944 °C). The oxygen fugacities of these eruptives (-10.5 to -9.9 log units and 1.2–1.4 log units above the FMQ buffer) are identical to those of the 2011 eruptives (-10.7 to -9.9 log units), except for 2011-1PP. 2018-4L3 showed the lowest temperature (868 °C) and the lowest oxygen fugacity (-11.2 log units) of the 2018 products.

The results of two-pyroxene thermometry and FeTi oxide thermometry applied to the 1716–17, 2011, and 2018 eruptions indicate that the temperature and oxidation state of the magma chamber did not change from 1716–17 to 2018. The lowest temperature 868 °C, which was obtained for 2018-4L3 with a dacite chemical composition (Table 2), is identical to the temperature estimated for the felsic magma end member (870 °C for a silicic andesite magma with 62–63 wt%  $SiO_2$ ) by Suzuki et al. (2013b). 2018-4L3 was therefore derived from the low-temperature silicic part of the magma chamber. 2011-2SWP, with a dacite chemical composition (Table 2), shows a relatively low temperature (908 °C), suggesting that it

originated in the low-temperature silicic part of the magma chamber and was heated by high-temperature magma before the eruption.

We then applied the olivine-liquid thermometer (Putirka 2008) to the chemical compositions of the melt and the host phenocrysts of 22 olivine-hosted melt inclusions from the 2011 products in order to estimate the temperature of the mafic end member magma that included olivine phenocrysts (Table 3; Additional file 4). Temperatures of 940–1041°C (average 990°C with standard deviation of  $\pm 25^\circ\text{C}$ ) were obtained, which is similar or slightly lower than the estimate for basaltic andesite magma obtained by Suzuki et al. (2013b). We also applied plagioclase-liquid thermometers (Putirka 2008) to the chemical compositions of the melt and the host phenocrysts of 10 plagioclase-hosted melt inclusions, clinopyroxene-liquid thermobarometers (Putirka 2008) to the chemical compositions of the melt and the host phenocrysts of 20 clinopyroxene-hosted melt inclusions, and orthopyroxene-liquid thermobarometers (Putirka 2008) to the chemical compositions of the melt and the host phenocrysts of 14 orthopyroxene-hosted melt inclusions (Table 3; Additional file 4). The temperature estimates for the plagioclase-, clinopyroxene-, and orthopyroxene-hosted melt inclusions in the 2011 products ( $938 \pm 23^\circ\text{C}$ ,  $951 \pm 18^\circ\text{C}$ , and  $978 \pm 36^\circ\text{C}$ , respectively) are similar to those obtained by the two-pyroxene thermometry (912–945 °C) and FeTi oxide thermometry (891–977 °C). In addition, the temperature estimates for the plagioclase-, clinopyroxene-, and orthopyroxene-hosted melt inclusions in the 2018 products ( $973 \pm 15^\circ\text{C}$ ,  $955 \pm 33^\circ\text{C}$ , and  $979 \pm 29^\circ\text{C}$ , respectively) are similar to those obtained by two-pyroxene thermometry (914–944 °C) and FeTi oxide thermometry (944–985 °C).

## Magma pressure

The large variability observed in the H<sub>2</sub>O and CO<sub>2</sub> contents of the andesite inclusions in the olivine phenocrysts and the dacite-rhyolite inclusions in the clinopyroxene- and orthopyroxene-phenocrysts from 2011 (Fig. 8) is not related to the SiO<sub>2</sub> content (Fig. 7), suggesting that magma degassing occurred with a decrease in the pressure. Gas saturation pressures were calculated from the H<sub>2</sub>O and CO<sub>2</sub> content of the inclusions by using the melt-H<sub>2</sub>O-CO<sub>2</sub> solubility models proposed by Newman and Lowenstern (2002) and Ghiorso and Gualda (2015) (Saito et al. 2018). Gas saturation pressures of 62–486 MPa (average of 232 MPa with standard deviation of  $\pm 132$  MPa,  $n = 22$ ) were obtained for the andesite inclusions in the olivine phenocrysts via the solubility model of Newman and Lowenstern (2002). The pressure range corresponds to a depth of 2–20 km under a lithostatic pressure gradient. Gas saturation pressures of 127–225 MPa (average of 182 MPa with standard deviation of  $\pm 36$  MPa,  $n = 9$ ) were calculated by the solubility model of Ghiorso and Gualda (2015), which is in the range of the estimates made using the solubility model of Newman and Lowenstern (2002). The pressure range corresponds to a depth of 5–9 km under a lithostatic pressure gradient. These results indicate that mafic magma ascended from a depth of at least 9 km to 2 km as the olivine crystallization occurred.

Large variability was also observed in the H<sub>2</sub>O and CO<sub>2</sub> contents of the dacite-rhyolite inclusions in the clinopyroxene- and orthopyroxene-phenocrysts from the 2011 products, which is not related to the SiO<sub>2</sub> content (Fig. 7), suggesting that magma degassing occurred alongside a decrease in pressure. Gas

saturation pressures were calculated using the H<sub>2</sub>O and CO<sub>2</sub> content obtained for the inclusions by the two melt-H<sub>2</sub>O-CO<sub>2</sub> solubility models. Gas saturation pressures of 36–199 MPa (average of 120 MPa with standard deviation of  $\pm 50$  MPa,  $n = 10$ ) were obtained via the solubility model of Newman and Lowenstern (2002). The average pressure (120 MPa) corresponds to a depth of 5 km under a lithostatic pressure gradient. Gas saturation pressures of 126–186 MPa (average of 152 MPa with standard deviation of  $\pm 25$  MPa,  $n = 5$ ) were calculated using the solubility model by Ghiorso and Gualda (2015), which is within the range obtained in the above estimates. These results indicate the presence of a felsic magma at a pressure of 120–152 MPa (corresponding to a depth of 5–6 km). The average gas saturation pressures obtained by the two solubility models ( $120 \pm 50$  MPa and  $152 \pm 25$  MPa) are in good agreement with the pressure estimated for silicic andesite magma (125 MPa) by Suzuki et al. (2013b).

Gas saturation pressures were similarly calculated using the H<sub>2</sub>O and CO<sub>2</sub> content of the andesite-rhyolite inclusions in the 2018 products and the above two melt-H<sub>2</sub>O-CO<sub>2</sub> solubility models. Gas saturation pressures of 74–205 MPa (average of 118 MPa with standard deviation of  $\pm 45$  MPa,  $n = 7$ ) were obtained using the solubility model by Newman and Lowenstern (2002), except for the extremely low gas saturation pressures observed in 18-1V-p2i1 and 18-1Vp4i1. The pressure range corresponds to a depth of 3–8 km under a lithostatic pressure gradient. The gas saturation pressures for the inclusions calculated by the solubility model by Ghiorso and Gualda (2015), were generally in the range 114–194 MPa (except for 18-1V-p2i1), with an average of 144 MPa and standard deviation of  $\pm 44$  MPa,  $n = 3$ , which is within the range of the above estimates. These estimates indicate that the 2018 magma was at depths of 3–8 km as the pyroxenes crystallized within the magma. The maximum estimate (8 km) is also similar to the source depth of the crustal deformation (7 km bsl) from July 2017 to March 2018 reported by JMA (2019b). The average gas saturation pressures estimated by the two solubility models ( $118 \pm 45$  MPa and  $144 \pm 44$  MPa) are the same as those estimated from the dacite-rhyolite inclusions in the 2011 products ( $120 \pm 50$  MPa and  $152 \pm 25$  MPa), indicating that the felsic magma was located at the same depth from 2011 to 2018.

Gas saturation pressures were also calculated using the H<sub>2</sub>O and CO<sub>2</sub> content of the dacite-rhyolite inclusions in 1716-17GP and the andesite-dacite inclusions in 1235S using the two melt-H<sub>2</sub>O-CO<sub>2</sub> solubility models. Gas saturation pressures of 71–106 MPa (average of 83 MPa with standard deviation of  $\pm 20$  MPa,  $n = 3$ ) were obtained for the dacite-rhyolite inclusions in 1716-17GP via the solubility model by Newman and Lowenstern (2002) while a pressure of 95 MPa was calculated for one plagioclase-hosted inclusion by the solubility model of Ghiorso and Gualda (2015). Extremely low gas saturation pressures were obtained for KP-p4i1. These results suggest that the 1716–17 magma was stored at a depth of 3–4 km. Gas saturation pressures of 89–136 MPa (average of 119 MPa with standard deviation of  $\pm 34$  MPa,  $n = 3$ ) and 117–122 MPa (average of 120 MPa with standard deviation of  $\pm 2$  MPa,  $n = 3$ ) were obtained for the andesite-dacite inclusions in 1235S using the solubility model of Newman and Lowenstern (2002). The results suggest that the 1235S magma was stored at a depth of 4–5 km. These results suggest that the magmas were generally stored at a depth of approximately 4 km before the eruptions.

# Bulk volatile content of magma

Suzuki et al. (2013b) concluded that a mafic magma, a basaltic-andesite magma with a temperature of 1030 °C and 9 vol% phenocrysts of olivine and plagioclase, was mixed with a felsic magma, a silicic-andesitic magma with a temperature of 870 °C and 43 vol% phenocrysts of plagioclase, pyroxene, and FeTi-oxide before the 2011 eruptions. The andesite inclusions in the olivine phenocrysts were likely derived from the mafic magma while the dacite-rhyolite inclusions in the pyroxene and plagioclase phenocrysts were sourced in the felsic magma. The H<sub>2</sub>O, S, and Cl contents of a melt in the 2011 mixed magma can be calculated from the volatile contents in the andesite and rhyolite inclusions, assuming that the melt was produced by the mixing of a melt from the mafic magma with a melt from the felsic magma (Table 4). The following assumptions were made; (1) inclusion 11-2SG-p9i1, with the highest H<sub>2</sub>O content of all the andesite inclusions from 2011-2SGP, can represent the mafic melt, (2) inclusion 11-2SG-p13i1, with the highest H<sub>2</sub>O content of all the rhyolite inclusions from 2011-2SGP, can represent the felsic melt, and (3) the mixed melt will have a SiO<sub>2</sub> content of 62 wt%, considering the SiO<sub>2</sub> content of 2011-2SGP (Additional file 5). This calculation gave a H<sub>2</sub>O content of 5.9 wt%, a S content of 0.107 wt%, and a Cl content of 0.066 wt% for the 2011 mixed melt. Based on the content in a phenocryst from 2011-2SGP (28 vol%), a bulk content of 4.0 wt% H<sub>2</sub>O, 0.072 wt% S, and 0.044 wt% Cl (Table 4) was obtained. Both the andesite inclusions in the olivine phenocrysts and the dacite-rhyolite inclusions in the pyroxene and plagioclase phenocrysts of the 2011 products have lower CO<sub>2</sub>/H<sub>2</sub>O mass ratios than those of the volcanic gas (Fig. 8). The disagreement in the CO<sub>2</sub>/H<sub>2</sub>O mass ratios of inclusions and volcanic gas is most likely due to the super-saturation of CO<sub>2</sub> at the time of inclusion entrapment. This indicates that merely measuring the melt inclusions might lead to underestimation of the total volatile content in the magmas, especially less-dissolved volatile species such as CO<sub>2</sub> (Papale, 2005). Because the volcanic gas observed in 2011 was emitted from a mixed magma, we calculated the bulk CO<sub>2</sub> content of the magma from the bulk H<sub>2</sub>O and S contents and the mass CO<sub>2</sub>/S and CO<sub>2</sub>/H<sub>2</sub>O ratios of the volcanic gas (Table 4). A bulk CO<sub>2</sub> content of 0.70 wt% was calculated from the bulk S content (0.072 wt%) and the mass CO<sub>2</sub> and S ratio in the volcanic gas (9.8; A1 magma in Table 4). A bulk CO<sub>2</sub> content of 0.14 wt% was thus calculated using the bulk H<sub>2</sub>O content (4.0 wt%) and the mass CO<sub>2</sub> and H<sub>2</sub>O ratio in the volcanic gas (0.035; A2 magma in Table 4).

Similar to the method used for the 2011 mixed magma, the H<sub>2</sub>O, S, and Cl contents of a melt in the 2018 magma were calculated from the volatile contents in the andesite and rhyolite inclusions, assuming that the mixed melt in the 2018 magma was composed of a mafic melt and a felsic melt (Table 4). The following assumptions were made; (1) inclusion 18-1V-p5i1, with the highest H<sub>2</sub>O content of all the inclusions in 2018-1VGP, can represent the mafic melt, (2) two felsic melts with low or high H<sub>2</sub>O contents were considered because the rhyolite inclusions are particularly varied in terms of H<sub>2</sub>O content (0.5–3.7 wt%); inclusion 18-1V-p1i1, with the highest H<sub>2</sub>O content of all the rhyolite inclusions in the 2018-1VGP represents felsic melt 1, and inclusion 18-1V-p2i1, with the lowest H<sub>2</sub>O content among all the rhyolite

inclusions in 2018-1VGP represents felsic melt 2, and (3) a mixed melt has a SiO<sub>2</sub> content of 65 wt%, considering the SiO<sub>2</sub> content of 2018-1VGP (Additional file 3). Mixing the 2018 mafic melt with 2018 felsic melt 1 gave a H<sub>2</sub>O content of 4.5 wt%, S content of 0.094 wt%, and Cl content of 0.091 wt% for 2018 mixed melt 1. Mixing the 2018 mafic melt with 2018 felsic melt 2 gave a H<sub>2</sub>O content of 2.1 wt%, S content of 0.082 wt%, and Cl content of 0.011 wt% for 2018 mixed melt 2. Based on the content of a phenocryst in 2018-1VGP (28 vol%), we obtained a B1 magma with a bulk content of 3.0 wt% H<sub>2</sub>O, 0.063 wt% S, and 0.060 wt% Cl and a B2 magma with a bulk content of 2.1 wt% H<sub>2</sub>O, 0.054 wt% S, and 0.054 wt% Cl (Table 4). Assuming super-saturation for CO<sub>2</sub> at the time of inclusion entrapment, we also calculated the bulk CO<sub>2</sub> content of the 2018 magma from the bulk S contents and the mass CO<sub>2</sub>/S ratio in the volcanic gas. A bulk CO<sub>2</sub> content of 0.10 wt% was obtained from the bulk S content (0.063 wt%) and the mass ratio of CO<sub>2</sub> and S in the volcanic gas in October 2017 (1.6; B1 magma in Table 4). A bulk CO<sub>2</sub> content of 0.087 wt% was calculated from the bulk S content (0.054 wt%) and the same mass ratio of CO<sub>2</sub> and S in the volcanic gas (B2 magma in Table 4).

In addition, the bulk H<sub>2</sub>O, S, and Cl contents (6.2 wt% H<sub>2</sub>O, 0.14 wt% S, and 0.050 wt% Cl) were estimated for the 2011 mafic magma from those of the 2011 mafic melt and phenocryst content (8.9 vol%) of the magma estimated by Suzuki et al. (2013b). The CO<sub>2</sub> content of the 2011 mixed melt was calculated at 1.0 wt% from the bulk CO<sub>2</sub> content of A1 magma and its phenocryst content (28 vol%). Assuming that the CO<sub>2</sub> content of the 2011 felsic melt was equal to that of inclusion 11-2SG-p13i1 (0.048 wt%), which is the maximum content in the rhyolite inclusions of the 2011 products, mass balance calculation gave a CO<sub>2</sub> content of 1.5 wt% for the mafic melt from the 2011 mixed melt and the mixing ratio (mafic:felsic = 0.67:0.33). The bulk CO<sub>2</sub> content of the 2011 mafic magma (M1 magma in Table 4) was calculated at 1.4 wt% considering the phenocryst content (8.9 vol%). In the same way, in terms of the A2 magma, this calculation gave a CO<sub>2</sub> content of 0.28 wt% for the mafic melt in the 2011 mixed melt comprising the A2 magma and the mixing ratio, resulting in a bulk CO<sub>2</sub> content of 0.25 wt% for the 2011 mafic magma (M2 magma in Table 4).

We could now estimate the bulk H<sub>2</sub>O, CO<sub>2</sub>, S, and Cl contents of the 2011 felsic magma, assuming that the H<sub>2</sub>O, CO<sub>2</sub>, S, and Cl contents of inclusion 11-2SG-p13i1 represent those of the felsic melt and no super-saturation of CO<sub>2</sub> occurred at the time the inclusions were entrapped. The bulk H<sub>2</sub>O, CO<sub>2</sub>, S, and Cl contents of felsic magma depend on the phenocryst content. Assuming that the felsic magma contained no phenocryst, a bulk content of 3.7 wt% H<sub>2</sub>O, 0.048 wt% CO<sub>2</sub>, 0.007 wt% S, and 0.087 wt% Cl were obtained ((F1 magma in Table 4). On the other hand, if the phenocryst content was 43 vol%, as estimated for silicic-andesite magma by Suzuki et al. (2013b), a bulk content of 1.9 wt% H<sub>2</sub>O, 0.025 wt% CO<sub>2</sub>, 0.004 wt% S, and 0.045 wt% Cl is obtained (F2 magma in Table 4).

## **Chemical composition of melt in the magma**

The chemical compositions of the groundmass in the 2018 products are slightly evolved as compared to the 2011 products (Fig. 4) in spite of the similarities in the whole-rock chemical composition and chemical compositions of the phenocrysts from the two masses. MELTS calculation (Gualda et al. 2012) was used to investigate the difference with the whole-rock composition of 2011-2SGP (Table 2) and a temperature of 928°C, pressures of 5–500 MPa, a FMQ + 2 buffer of  $fO_2$ , and the bulk  $H_2O$  and  $CO_2$  contents of the A1 and A2 magmas (4.0 wt%  $H_2O$  and 0.70 wt%  $CO_2$  or 0.14 wt%  $CO_2$ ; Additional file 8). The MELTS calculations indicate the presence of crystallized plagioclase, clino- and ortho-pyroxene, and FeTi-oxide phenocrysts without any olivine phenocrysts (Additional file 8). The gas saturation pressures for the dacite-rhyolite inclusions in the 2011 products (36–199 MPa) that were obtained in the previous section suggest that the pressure in the 2011 felsic magma chamber was 50–200 MPa. Melts in the A1 and A2 magmas have  $SiO_2$  contents ranging from 65.37–71.48 wt% with 2.28–3.64 wt%  $K_2O$  at pressures of 50–200 MPa (Fig. 4). These chemical compositions are slightly  $SiO_2$ - and  $K_2O$ -rich compared to the groundmass in the 2011 products (Fig. 4). Tomiya et al. (2013) proposed that the injection of mafic magma into the chamber occurred several weeks to several days before the 2011 subplinian eruptions. Therefore, the difference between the chemical composition of the melts in the A1 and A2 magmas and the groundmass occurred because the 2011 mixed magma had not reached chemical equilibrium due to the short time period between mixing and eruption.

The MELTS calculation was also applied to the whole-rock composition of 2018-1VGP (Table 2) with a temperature of 944°C, pressures of 5–500 MPa, a FMQ + 2 buffer of  $fO_2$ , and the bulk  $H_2O$  and  $CO_2$  contents of the B1 and B2 magmas (3.0 wt%  $H_2O$  and 0.10 wt%  $CO_2$  for B1 magma, 2.1 wt%  $H_2O$  and 0.087 wt%  $CO_2$  for B2 magma; Additional file 8). The MELTS calculation indicated crystallization of the plagioclase, clino- and ortho-pyroxene, and FeTi-oxide phenocrysts (Additional file 8) with melts containing  $SiO_2$  contents of 66.31–70.76 wt% and 2.43–3.40 wt%  $K_2O$  at pressures of 50–200 MPa. These chemical compositions are similar to the results for the A1 and A2 magmas and are similar or slightly  $SiO_2$ - and  $K_2O$ -rich compared to the groundmass in the 2018 products, except for that obtained for FeO (Fig. 4). The similar chemical compositions obtained for the groundmass in the 2018 products and the melts obtained by the MELTS calculation suggest that the 2018 magma was closer to chemical equilibrium. This suggests that the mixed magma from 2011 remained in the magma chamber and that the chemical reactions between the minerals and melt produced the 2018 magma. The rarity of olivine phenocrysts and lack of existence for groundmass olivines in the 2018 products support this hypothesis because the results of the MELTS calculation indicate that olivines could not crystallize in the A1, A2, B1, and B2 magmas. The olivine phenocrysts that originated in the 2011 mafic magma, which were injected into the 2011 felsic magma, were probably dissolved in the mixed magma over time. The increase in the fractions of plagioclase phenocrysts with wide rims of >0.1 mm, and clinopyroxene and orthopyroxene phenocrysts with wide rims of >0.05 mm from the 2011 magma to the 2018 magma (mentioned previously), also supports this hypothesis.

In order to evaluate this hypothesis, compositional profiles from the core to the rim of 13 orthopyroxene phenocrysts from 2011-1PP to 2011-7VL and 12 orthopyroxene phenocrysts from 2018-1VGP and 2018-

1VS were measured, all of which show rims with reverse zoning under EPMA (Additional file 2). The compositional profiles of the orthopyroxene phenocrysts in the 2011 products show a large change in the Mg# at a distance of 0.02–0.03 mm from the rims, with widths of less than 0.005 mm. The Mg# profiles were calculated via Mg-Fe diffusion (Saunders et al. 2012) using a residence time of 1, 10, and 100 years at a temperature of 928 °C. The observed Mg# profiles were similar to those obtained for 1 year using the calculation (Additional file 2). On the other hand, the compositional profiles of the orthopyroxene phenocrysts in the 2018 products show a large change in the Mg# at a distance of 0.04–0.10 mm from the rims. The widths of the Mg# range from 0.010 to 0.028 mm, which is larger than those obtained for the 2011 products, suggesting that Mg and Fe diffusion continued over this time period. The observed Mg# profiles appear to be closer to those obtained for 10 years by calculation (Additional file 2). Therefore, the observed compositional profiles of the core to rim of orthopyroxene phenocrysts in the 2011 and 2018 products are consistent with the above hypothesis, although more detailed analysis is needed in the future.

## Bubble volume and magma density

The density contrast between magma and crust can control the ascent of magma; magma can become trapped within a magma chamber if the density contrast becomes negligible (e.g., Walker 1989). In addition, the bubble volume of magma can control its eruption style; magmas with high bubble volume cause explosive eruptions, while those with poor in bubble volume lead to effusive eruptions. We therefore need to obtain the bubble volume and the density of the magma to investigate the magma ascent and eruption processes. Both bubble volume and magma density are highly dependent on the bulk volatile content of a magma. Assuming that the gas bubbles that formed by the exsolution of H<sub>2</sub>O and CO<sub>2</sub> from the melt did not separate from the magma during its ascent, the bubble volume and densities of the mafic and felsic magmas of the 2011 eruptions, the 2011 mixed magma, and the 2018 magma at different depths were calculated using the bulk H<sub>2</sub>O and CO<sub>2</sub> contents of the magma (Saito et al., 2018). Details of the calculation methods are given in Additional file 8 and Additional file 4 of Saito et al. (2018).

The conditions used for calculation of the 2011 mafic magmas (M1 and M2 magmas) were as follows; whole-rock composition and temperature of 1030°C of basaltic-andesite magma estimated by Suzuki et al. (2013b), an oxygen fugacity controlled by the NNO buffer, and the bulk H<sub>2</sub>O and CO<sub>2</sub> contents of the M1 and M2 magmas (Table 4). The major-element compositions of the mafic melts at pressures of 50–500 MPa are similar to those of the andesite inclusions in the olivine phenocryst (Fig. 6). The H<sub>2</sub>O and CO<sub>2</sub> contents of the mafic melts at pressures of 50–500 MPa are also similar to the distribution of the andesite inclusions (Figs. 7c, 7d and 8a). These similarities indicate that the calculation results are close to the actual conditions. The calculation indicates that the mafic magmas (M1 and M2) had bubble volumes of 12.7–19.7 vol% and densities of 1987–2144 kg m<sup>-3</sup> at a pressure of 200 MPa, indicating that mafic magma contained abundant bubbles and was of low density before it was injected into the felsic magma.

The conditions used for calculation of the 2011 felsic magmas (F1 and F2 magmas) were; a whole-rock composition of 2011-2SWP, the temperature of 870°C for silicic-andesite magma estimated by Suzuki et al. (2013b), an oxygen fugacity controlled by 2 log units above the FMQ buffer, and the bulk H<sub>2</sub>O and CO<sub>2</sub> contents of the F1 and F2 magmas (Table 4). The major-element compositions of the felsic melts at pressures of 50–200 MPa are similar to those of the dacite-rhyolite inclusions in the 2011 products (Fig. 6). The H<sub>2</sub>O and CO<sub>2</sub> contents of the felsic melts at pressures of 50–200 MPa are also similar to the distribution in the dacite-rhyolite inclusions (Figs. 7c, 7d and 8a). The calculation indicates that the felsic magmas (F1 and F2) had bubble volumes of < 8.4 vol% and densities of 2264–2496 kg m<sup>-3</sup> at a pressure of 125 MPa (Additional file 8), which is the pressure of the felsic magma chamber estimated using the gas saturation pressures for dacite-rhyolite inclusions in the 2011 products. Because the mafic magmas had lower densities of 1717–1835 kg m<sup>-3</sup> than the felsic magma at the same pressure, the density contrast may have caused the two magmas to mingle and mix.

These calculations also provide information about the bubble volume and density of the 2011 mixed magma. Assuming that the chemical equilibrium obtained for the mixed magma is correct, the 2011 mixed magma (A1 and A2 magmas) had a bubble volume of 3.2–9.2 vol% and a density of 2280–2401 kg m<sup>-3</sup> at a pressure of 200 MPa, and 48.1–50.4 vol% and 1348–1402 kg m<sup>-3</sup> at a pressure of 50 MPa. However, the difference between the chemical composition of the groundmass and that obtained by the MELTS calculation for the 2011 products reveals that the mixed magma had not attained chemical equilibrium upon eruption. Consequently, the above estimation for the A1 and A2 magmas might be an extreme example. Therefore, we calculated the bubble volume and density of the mixed magmas M1 (or M2) and F1 (or F2) by using the mass ratio for each magma in the mixing process (M1 or M2 : F1 or F2 = 0.65:0.35; Additional file 9). This case defines the other extreme in which the two magmas simply “mingled” without any chemical reaction. The bubble volume and density of the mixed M1 + F1 magma are 13.8–57.1 vol% and 1162–2118 kg m<sup>-3</sup> at pressure ranges of 50–200 MPa while those of the M2 + F2 magma are 13.8–53.5 vol% and 1162–2147 kg m<sup>-3</sup>, respectively, at the same pressure ranges (Fig. 9; Additional file 9). These calculations indicate that the 2011 mixed magma had a high-volume content of approximately 50 vol% at a low pressure of 50 MPa, whether chemical equilibrium was attained in the magma or not.

We also calculated the bubble volume and density of the 2018 magma, assuming that chemical equilibrium was attained in this magma. The 2018 magma (B1 and B2 magmas) had a bubble volume of 0.5–1.1 vol% and a density of 2483–2549 kg m<sup>-3</sup> at a pressure of 200 MPa, and 24.4–37.4 vol% and 1657–1983 kg m<sup>-3</sup> at 50 MPa. The bubble volume of the 2018 magma (24.4–37.4 vol%) at a pressure of 50 MPa is smaller than those calculated for the M1 + F1 and M2 + F2 magmas (53.5–57.1 vol%) and the A1 and A2 magmas (48.1–50.4 vol%) at the same pressure (Fig. 9). The lack of subplinian eruptions in 2018 is therefore considered to have been because of the low bubble volume in the shallow part of the magma at this time.

# Degassed-magma Volume

The mass of degassed magma during volcanic activity is one of the important factors used in investigating the degassing process. We calculated the mass of degassed magma based on the estimated bulk volatile content of the 2011 and 2018 magmas, the measured SO<sub>2</sub> flux, and the chemical composition of the magmatic gas emitted from the summit crater, using the equation:

$$M_{VE} = (C_{MM} - C_{DM}) \times M_{DM},$$

where  $M_{DM}$  is the mass of degassed magma (kg),  $C_{MM}$  is the bulk volatile content of the mixed magma (kg kg<sup>-1</sup>),  $C_{DM}$  is the bulk volatile content of the degassed magma (kg kg<sup>-1</sup>), and  $M_{VE}$  is the mass of the volatile material emitted from the summit crater (kg). The bulk volatile content of 0.072 wt% S and 0.044 wt% Cl (Table 4) that was obtained for the A1 (or A2) magma ( $C_{MM}$ ) was used to calculate the mass of degassed magma in 2011–12. The volatile content of degassed magma ( $C_{DM}$ ) was estimated from the S and Cl contents of the groundmass in the 2011 products (Additional file 3), assuming phenocryst contents of 28 vol% and no S or Cl contents in the phenocrysts. The mass of emitted sulfur was calculated from the SO<sub>2</sub> flux and the mole ratio of SO<sub>2</sub>/H<sub>2</sub>S (Additional file 10). The mole ratio was 8 on 15 March 2011, before decreasing to 0.8–3.3 after April (Shinohara 2013). Mole ratios of 8 and 2 were therefore assumed for these periods, respectively. The H<sub>2</sub>O/SO<sub>2</sub> and CO<sub>2</sub>/SO<sub>2</sub> ratios were assumed to be 560 and 8 (Shinohara 2013) and a Cl/S ratio of 0.235 was based on the ratio in the ash-leachate (Vinet N Person. Communication). The mass of degassed magma (kg) was then converted to the degassed-magma volume (x10<sup>6</sup> m<sup>3</sup>) for comparison with the erupted-magma volume and crust deformation, assuming a magma density of 2500 kg m<sup>-3</sup>. The mass of the degassed magma in 2017–18 were also calculated for two cases in which the magma had (1) the bulk S content of the B1 magma (0.063 wt% S) and (2) the bulk S content of the B2 magma (0.054 wt% S) before degassing (Table 4). The bulk S content of the magma after degassing was calculated from the minimum S content of the groundmass (0.002 wt% of 2018-4L1 in Additional file 3) and the phenocryst content (28 vol%) of the 2018 products. The mole ratio of SO<sub>2</sub> and H<sub>2</sub>S in the volcanic gas was assumed to be 2.7 based on observation of the volcanic gas (Additional file 10). A detailed description of the calculation used for the degassed magmas is given in Table 5 and Additional file 10. If the average, minimum, and maximum SO<sub>2</sub> flux values are observed over a single day, the maximum value is at most two times larger and the minimum value 0.3 times larger than the average (Additional file 10). This indicates that an error of 30–200% for the degassed-magma volume is unavoidable.

The degassed-magma volume in 2011–12 is summarized for four periods, depending on the eruption style (Table 5). The degassed-magma volume on 26–27 January (4–5 × 10<sup>6</sup> m<sup>3</sup>) is smaller than the volume of magma that was erupted (7–11 × 10<sup>6</sup> m<sup>3</sup>; Maeno et al. 2014) during the subplinian eruptions on 26–27 January. However, the estimation that was used to obtain the volume of degassed magma is likely to have been underestimated, because no SO<sub>2</sub> flux measurement was made during the most active

periods of eruption. The volume of degassed magma on 28 January–1 February ( $24\text{--}32 \times 10^6 \text{ m}^3$ ) was 1.6–2.1 times larger than that of erupted magma in the same period ( $15 \times 10^6 \text{ m}^3$ ; Kozono et al. 2013; Nakada et al. 2013). Considering the error in the  $\text{SO}_2$  flux measurement mentioned above, the degassed-magma volume is likely consistent with erupted-magma volume. This indicates that the  $\text{SO}_2$  gas emission on 28 January–1 February could be explained by degassing of the lava effused in the summit crater. On the other hand, the degassed-magma volume on 2 February–7 September ( $13\text{--}18 \times 10^6 \text{ m}^3$ ) is more than 65 times greater than that of the erupted magma in the same period (less than  $0.2 \times 10^6 \text{ m}^3$ ; Nishiki et al. 2013). Furthermore, during the period 8 September 2011–26 September 2012, approximately  $2\text{--}3 \times 10^6 \text{ m}^3$  of magma was degassed although none was erupted. The excess degassing during the period 2 February 2011–26 September 2012 indicates that the magmatic gas was derived from the non-erupted magma located in a deeper part of the chamber. Because the magma chamber is located at a depth of approximately 5 km (Suzuki et al. 2013b), such degassing may be due to magma convection in a conduit (Ohwada et al. 2013; Shinohara 2013). This excess degassing may have decreased the bulk volatile content of the 2011 magma in the chamber over time.

GPS observation indicates that deflation reaching  $14 \times 10^6 \text{ m}^3$  occurred between 25 January and 1 February, which could be explained by the discharge of magma from the chamber to the surface (Nakada et al. 2013). The crustal deflation changed to inflation on 25 February, and this continued until December 2011. GPS observation indicates that the total volume of the inflation was  $11 \times 10^6 \text{ m}^3$  (Table 5). The inflation could be explained by continuous replenishment of the magma chamber from a deep source (Nakada et al. 2013; Nakao et al. 2013; Suzuki et al. 2013b). The mafic-magma proportion of the degassed magma on 2 February 2011–26 September 2012 could be  $10\text{--}14 \times 10^6 \text{ m}^3$  using a mixing ratio of 0.65 for mafic to mixed magma (Suzuki et al. 2013b) and a degassed-magma volume of  $15\text{--}21 \times 10^6 \text{ m}^3$  (Table 5). This estimate is similar to the inflation of the chamber observed by GPS, suggesting that mafic magma was injected to the chamber from deeper in the volcano during February–December 2011, causing inflation of the crust, gas emission, and small eruptions.

The degassed-magma volume in 2017–18 is summarized for five periods, depending on the kind of eruption that occurred (Table 5). The degassed-magma volume estimated for 11 October 2017–28 February 2018 ( $14 \times 10^6 \text{ m}^3$ ) is much larger than the erupted-magma during this period. The degassed-magma volume for 1 March–9 March ( $29 \times 10^6 \text{ m}^3$ ) is 1.9–2.2 times greater than the magma erupted in the same period ( $15 \times 10^6 \text{ m}^3$ ; Chiba et al. 2018). Considering the error in the  $\text{SO}_2$  flux measurement, the degassed-magma volume on 1 March–9 March ( $29 \times 10^6 \text{ m}^3$ ) is similar to the volume of erupted magma, indicating that all the  $\text{SO}_2$  gas emitted in the summit crater was derived from the lava erupted during this period. On the other hand, the degassed-magma volume for 10 March–27 June ( $5 \times 10^6 \text{ m}^3$ ) is 17–20 times larger than erupted-magma volume in the same period ( $0.3 \times 10^6 \text{ m}^3$ ; Oikawa et al. 2018). Furthermore,  $3 \times 10^6 \text{ m}^3$  of magma was degassed from 28 June–13 October 2018, although no magma was erupted. Similar to 2011–12, a large degassed magma volume that was greater than the erupted magma volume was observed in a period of vulcanian eruptions occurred alongside ash and gas

emissions, suggesting that the degassing occurred by convection in a conduit (Ohwada et al. 2013; Shinohara 2013). GPS observation indicates that the deflation of the crust after 1 March reverted to inflation on 10 March and that the inflation continued until January 2019, with a total volume of  $10 \times 10^6 \text{ m}^3$  (Table 5). As discussed for 2011–12, the magma chamber must have undergone replenishment from a deep source during this period, causing inflation of the crust, gas emission, and small eruptions.

## Ascent And Degassing Processes Of The Magma

Based on the above estimation of the physical and chemical conditions in the magmas and the degassed-magmas, the magma ascent- and degassing processes were estimated for the 2011 and 2017–18 Shinmoedake eruptions. The subplinian eruptions in January 2011 were the result of mixed mafic- and felsic magma. The mafic magma had basaltic-andesite composition while the felsic magma had silicic-andesite composition, and the proportion of basaltic-andesitic magma in the mixed magma ranged from 0.6 to 0.7 (Suzuki et al. 2013b). The felsic magma must have been stored at a pressure of 120–152 MPa (equivalent to a depth of 5–6 km), considering the gas saturation pressures for the dacite-rhyolite inclusions in the 2011 products that were obtained using the two solubility models ( $120 \pm 50 \text{ MPa}$  and  $152 \pm 25 \text{ MPa}$ ). The felsic magma had relatively lower bulk volatile content (1.9–3.7 wt%  $\text{H}_2\text{O}$ , 0.025–0.048 wt%  $\text{CO}_2$ , 0.004–0.007 wt% S, and 0.045–0.087 wt%; Table 4), bubble volumes of < 9.3 vol%, and a bulk density of  $2241\text{--}2496 \text{ kg m}^{-3}$  at 125 MPa (Fig. 9). The density structure beneath Shinmoedake is estimated to be  $2000\text{--}2500 \text{ kg m}^{-3}$  at depths of less than 0 km bsl and approximately  $2500 \text{ kg m}^{-3}$  at depths of 0–1 km bsl (JMA, 2013). Assuming that the density of the crust is  $2500 \text{ kg m}^{-3}$  at depths of more than 0 km bsl, the felsic magma may not be able to ascend to shallower depths because of the small contrast between the density of the felsic magma and the crust. Considering that the major-element composition of 1716–17WP is similar to that of 2011-2SWP (Table 2; Fig. 2), which was likely derived from the felsic magma, the felsic magma can be assumed to have remained in the chamber following the 1716–17 eruptions.

The mafic magma with bulk volatile content of 6.2 wt%  $\text{H}_2\text{O}$  and 0.25–1.4 wt% of  $\text{CO}_2$  may have ascended from a depth of 19 km (at a pressure of 486 MPa) based on the gas saturation pressures of the andesite inclusions in the olivines from the 2011 products ((i) in Fig. 9). The mafic magma had bubble volumes of 27.6–33.0 vol% and densities of  $1717\text{--}1835 \text{ kg m}^{-3}$  at 125 MPa (M1 and M2 in Additional file 8). The lower density of the mafic magma than the felsic magma ( $2241\text{--}2496 \text{ kg m}^{-3}$ ; Fig. 9: Additional file 8) suggests that it may have injected into the felsic magma chamber, promoting mixing of the two magmas ((ii) in Fig. 9). Comparison between the results of the MELTS calculation and the chemical composition of the groundmass in the 2011 products indicates that the mixed magma did not attain chemical equilibrium before eruption. Densities of  $1875\text{--}2022 \text{ kg m}^{-3}$  for the M1 + F1 and M2 + F2 magmas and  $2050\text{--}2147 \text{ kg m}^{-3}$  for the A1 and A2 magmas were obtained at a pressure of 125 MPa. Both densities are lower than that of the surrounding felsic magma at the same pressure ( $2241\text{--}2496 \text{ kg m}^{-3}$ ; Fig. 9), suggesting that the mixed magma may have continued ascending ((iii) in Fig. 9).

Furthermore, the ascending mixed magma had bubble volumes of 51.3–57.1 vol% (M1 + F1 and M2 + F2 magmas; density of 1186–1222 kg m<sup>-3</sup>) or 48.1–50.4 vol% (A1 and A2 magmas; density of 1348–1402 kg m<sup>-3</sup>) at a pressure of 50 MPa. Such bubble-rich magma could have caused the subplinian eruptions. We should mention here that the above densities and the bubble volumes were calculated with the assumption that gas bubbles that formed from the exsolution of H<sub>2</sub>O and CO<sub>2</sub> from the melt do not separate from the magma during its ascent. If the bubbles separated from the magma and rose up to an upper part of the chamber, the magma erupted at the subplinian eruptions could have a higher bubble volume than the above estimates. The chemical composition of the groundmass in March–August 2011 seems more evolved than that in January–February, and becomes close to that predicted by MELTS for a melt in the mixed magma, indicating that the chemical reaction partially proceeded in the magma during the period March–August. On the other hand, the volume of degassed-magma from 2 February 2011 to September 2012 was more than 75 times greater than that of the eruptive products during the same period. This suggests that the magma in the chamber underwent degassing due to the convection of magma in a conduit. This excess degassing may have decreased the bulk volatile content in the 2011 magma.

The similar whole-rock composition and variations in the plagioclase-, clinopyroxene-, and orthopyroxene-phenocryst cores of the 2011 and 2018 magmas indicates that the 2011 mixed magma remained following eruption. Similar gas saturation pressures (with averages of 118 ± 45 MPa and 144 ± 44 MPa by the two solubility models) were obtained from the H<sub>2</sub>O and CO<sub>2</sub> contents of the andesite-rhyolite inclusions in the 2018 products, indicating that the depth of the magma chamber did not change from 2011 to 2018. However, the rarity of the olivine phenocrysts, wide rims of plagioclase, clinopyroxene and orthopyroxene phenocrysts in the 2018 products and the comparison between the MELTS calculation and the groundmass in the 2018 products indicates that that chemical reaction of the magma proceeded to reach equilibrium. The estimated bulk volatile contents for the 2018 magma (3.0 wt% H<sub>2</sub>O and 0.10 wt% CO<sub>2</sub> for B1 magma and 2.1 wt% H<sub>2</sub>O and 0.087 wt% CO<sub>2</sub> for B2 magma; Table 4) are lower than those obtained for the 2011 magma. The decrease in the volatile content may have been caused by the excess degassing of the 2011 magma in the magma chamber following the eruptions. The density of the 2018 magma was 2374–2498 kg m<sup>-3</sup> at a pressure of 125 MPa, which is similar to that of the surrounding felsic magma (2241–2496 kg m<sup>-3</sup>; Fig. 9). Considering the small contrast between the density of the 2018 magma and the surrounding felsic magma, the 2018 magma may not have ascended via buoyancy. Instead, the injection of new magma into the bottom of the 2018 magma chamber, inferred from the crust inflation from June 2017 to March 2018 (JMA 2019b), may have forced the 2018 magma into shallower depths, resulting in the 2018 eruptions. We speculate that the new magma had relatively low bulk volatile content because if the magma had high volatile content like the 2011 mafic magma, it could have turned over to mix with the 2018 magma before eruption. The lower bubble volume of the 2018 magma (24.4–37.4 vol% at 50 MPa) is likely to have led to effusive rather than explosive eruption. After the lava effusion in March 2018, the volume of degassed magma present was greater than the volume of erupted magma (more than 27-fold), suggesting the degassing of magma by convection in a

conduit. GPS observation indicates a total volume of  $10 \times 10^6 \text{ m}^3$  for the inflation that occurred from 10 March to 31 January 2019 (Table 5), suggesting that new magma injected into the chamber from greater depths caused the degassing activity.

## Summary And Conclusions

(a) Petrological observation and melt-inclusion analysis of products from the 2011 and 2018 eruptions at Shinmoedake in the Kirishima volcanic group were conducted to investigate the magma ascent and degassing processes. Whole-rock composition and chemical compositions of plagioclase-, clinopyroxene-, and orthopyroxene-phenocryst cores from the 2018 products were found similar to those in the 2011 products, suggesting that the 2018 magma was a remnant of the 2011 magma. Comparison of the mode composition and chemical composition of the groundmass in the 2018 products with the results obtained using MELTS indicates that the magma approached chemical equilibrium between 2011 and 2018, suggesting that the changes observed could be explained by the magma approaching chemical equilibrium.

(b) Melt-inclusion analysis reveals that the inclusions obtained for the 2011 eruptions can be divided into two types; andesite inclusions in olivine phenocrysts and dacite-rhyolite inclusions in plagioclase, clinopyroxene, and orthopyroxene phenocrysts. Large variations were observed in the volatile content of the andesite and dacite-rhyolite inclusions, which are uncorrelated with the  $\text{SiO}_2$  or  $\text{K}_2\text{O}$  contents in the inclusions, indicating degassing of the andesite and dacite-rhyolite melt. The inclusions from the 2018 eruptions have andesite to rhyolite compositions with no gaps in the chemical compositions. Large variations are also observed in the  $\text{H}_2\text{O}$ , S, and Cl contents of the andesite-rhyolite inclusions from the 2018 eruptions, which are roughly correlated with the  $\text{SiO}_2$  contents of the inclusions, indicating that mafic melt with high  $\text{H}_2\text{O}$ , S, and Cl contents was mixed with felsic melt of low  $\text{H}_2\text{O}$ , S, and Cl contents.

(c) Two-pyroxene thermometry (Putirka 2008) was applied to the compositions of the borders of intergrown clinopyroxene and orthopyroxene phenocrysts from the 1716–17, 2011, and 2018 eruptions, with results indicating that the temperature of the 2018 magma was similar to those of both the 2011 and the 1716–17 magmas. The application of FeTi oxide thermometry to the compositions at the borders of the intergrown magnetite and ilmenite phenocrysts from the 2018 products gave temperature and oxygen fugacity estimates similar to those obtained for the 2011 and 1716–17 magmas. These results indicate that the temperature and oxidation state of the magma chamber did not change from 1716–17 to 2018.

(d) Gas saturation pressures of the andesite inclusions in the 2011 products calculated using the  $\text{H}_2\text{O}$  and  $\text{CO}_2$  content range from 62 to 486 MPa (with averages of  $232 \pm 132$  MPa and  $182 \pm 36$  MPa from the two solubility models). The gas saturation pressures of the dacite-rhyolite inclusions in the 2011 products range from 62 to 199 MPa and the averages obtained using the two solubility models ( $120 \pm 50$  MPa and  $152 \pm 25$  MPa) are in good agreement with an estimate (125 MPa) for silicic-andesite magma made by Suzuki et al. (2013b). The gas saturation pressures of the andesite-rhyolite inclusions in the 2018

products range from 74 to 205 MPa (averages of  $118\pm 45$  MPa and  $144\pm 44$  MPa by the two solubility models), which is similar to the estimation made for the 2011 felsic magma.

(e) The bulk volatile contents of the magmas associated with the 2011 and 2018 eruptions were estimated based on the volatile content of the melt inclusions and the chemical composition of volcanic gas; the 2011 mixed magma showed 4 wt% H<sub>2</sub>O and 0.70–0.14 wt% CO<sub>2</sub>, 2011 mafic magma showed 6.2 wt% H<sub>2</sub>O and 1.4–0.25 wt% CO<sub>2</sub>, 2011 felsic magma showed 3.7–1.9 wt% H<sub>2</sub>O and 0.048–0.025 wt% CO<sub>2</sub>, and 2018 magma showed 3.0–2.1 wt% H<sub>2</sub>O and 0.10–0.087 wt% CO<sub>2</sub>.

(f) The bubble volume and density of the mafic and felsic magmas from the 2011 eruptions, 2011 mixed magma, and 2018 magma were calculated at pressure ranges of 5–500 MPa using the bulk volatile content and whole-rock composition of the magmas. The calculation shows that the mafic magmas were of lower density than the felsic magma, and that the mafic magma rose into the felsic magma within the magma chamber, promoting mixing. The 2011 magma had a particularly high bubble volume just before eruption (about 50 vol% at a pressure of 50 MPa), which caused the subplinian eruption. The 2018 magma had a lower bubble volume (24.4–37.4 vol% at a pressure of 50 MPa) and thus failed to cause subplinian eruptions.

(g) The mass of degassed magma present was calculated based on the estimated volatile content of the magma, the measured SO<sub>2</sub> flux, and the chemical composition of the magmatic gas emitted from the summit crater. The degassed-magma volume from 2 February 2011 to September 2012 was more than 75 times as large as that of the eruptive products during the same period, suggesting that the degassing of magma in the chamber was due to magma convection in a conduit. This excess degassing decreased the bulk volatile content of the 2011 magma.

(h) The magma ascent and degassing processes of the 2011 and 2017–18 Shinmoedake eruptions are also proposed. Mafic magma with a high volatile content of 6.2 wt% H<sub>2</sub>O and 1.4–0.25 wt% CO<sub>2</sub> ascended from at a depth of 19 km before the 2011 eruptions. The mafic magma, with high bubble volume and low density, was injected into and mixed with the felsic magma located at a depth of 5–6 km. The bubble volume of the mixed magma increased to approximately 50 vol% at a depth of 2 km, followed by fragmentation, and resulted in subplinian eruptions on 26–27 January 2011. Degassing of the magma in the chamber due to magma convection in a conduit started in March 2011, together with small eruptions. This excess degassing may have decreased the bulk volatile content of the magma. The mixed magma then proceeded towards chemical equilibrium. The 2018 magma, with a low volatile content of 2.1–3.0 wt% H<sub>2</sub>O and 0.087–0.13 wt% CO<sub>2</sub>, ascended again from the magma chamber, probably due to the injection of new magma into the bottom of the chamber, which likely started in 2017. This magma, with relatively low bubble content, could not cause a subplinian eruption and erupted instead via effusion in March 2018.

## Abbreviations

AIST: Advanced Industrial Science and Technology

BSE: Backscattered electron

bsl: below sea level

CD: Volatile content of the degassed magma

CM: Volatile content of the magma

DRE: Dense rock equivalent

EPMA: Electron probe micro analyzer

GSJ: Geological Survey of Japan

MD: Mass of degassed magma

MV: Mass of volatile material emitted from the crater

SEM: Scanning Electron Microscopy

SIMS: Secondary Ion Mass Spectrometry

XRF: X-ray fluorescence analysis

## **Declarations**

### **Ethics approval and consent to participate**

Not applicable.

### **Consent for publication**

Not applicable.

### **Availability of data and materials**

The datasets used and/or analysed during the current study are available from the corresponding author on reasonable request.

### **Competing interests**

The authors declare no competing interests.

### **Funding**

Not applicable.

### **Authors' contributions**

GS carried out the SEM, EPMA, and SIMS analyses of the eruptive products and the Melts calculation and drafted the manuscript.

TO performed the geological survey of the 2018 eruption at Shinmoedake, Kirishima volcano group and collected the samples.

OI carried out the whole-rock analyses of the eruptive products.

All authors read and approved the final manuscript.

### **Acknowledgements**

We thank Dr. Nicolas Vinet for providing data on the Cl/S ratio of ash-leachate from the Shinmoedake eruption. We thank Drs. Nobuo Geshi, Yoshihiro Ishizuka, Ryuta Furukawa, and Masayuki Oishi for providing the rock samples used in this research and their helpful comments. We thank Dr. Isoji Miyagi for helping SIMS measurements. We would like to thank Editage ([www.editage.jp](http://www.editage.jp)) for English language editing.

### **Authors' information**

All authors are researchers at the Geological Survey of Japan, AIST.

## **References**

1. Anderson AT (1973) The before-eruption water content of some high-alumina magmas. *Bull Volcanol* 37:530–552
2. Anderson AT, Newman S, Williams SN, Druitt TH, Skirius C, Stolper E (1989) H<sub>2</sub>O, CO<sub>2</sub>, Cl, and gas in plinian and ash-flow Bishop rhyolite. *Geology* 17:221–225
3. Anderson D, Lindsley DH, Davidson P (1993) QUILF: A pascal program to assess equilibria among Fe-Mg-Mn-Ti oxides, pyroxenes, olivine, and quartz. *Computers Geosci* 19:1333–1350
4. Cherniak DJ, Dimanov A (2010) Diffusion in Pyroxene, Mica and Amphibole. *Reviews in Mineralogy & Geochemistry*, 72, Diffusion in Minerals and Melts. Mineralogical Society of America, pp 641–690
5. Chiba T, Oikawa T, Sasaki H, Hirakawa Y, Miyabuchi Y, Nakada S (2018) Topography of the 2018 lava flow from Shinmoedake crater, Kirishima Volcanoes, Kyushu, Japan. In: Abstracts of Volcanol Soc Japan 2018 Fall Meeting (in Japanese), A1-01, Akita, Japan, 26–30 September 2018
6. Geological Survey of Japan, Agency of Industrial Science and Technology (2017) Report on volcanic gas observation at Shinmoedake, Kirishima volcanoes on 12 October 2017. Paper presented at a

- meeting of Coordinating Committee for Prediction of Volcanic Eruption, 19 October 2017 (in Japanese)
7. Gerlach TM, Westrich HR, Symonds RB (1996) Preruption vapor in magma of the climactic Mount Pinatubo eruption: Source of the giant stratospheric sulfur dioxide cloud. In: Newhall CG, Punongbayan RS (eds) Fire and mud: eruptions and lahars of Mount Pinatubo, Philippines, Univ Washington Press, pp 415–433
  8. Geshi N, Takarada S, Tsutsui M, Mori T, Kobayashi T (2010) Products of the August 22, 2008 eruption of Shinmoedake Volcano, Kirishima Volcanic Group, Japan. Bull Volcanol Soc Jpn 55:53–64 (in Japanese with English abstract)
  9. Ghiorso MS, Gualda GAR (2015) An H<sub>2</sub>O-CO<sub>2</sub> mixed fluid saturation model compatible with rhyolite-MELTS. Contrib Miner Petrol. doi:10.1007/s00410-015-1141-8
  10. Gualda GAR, Ghiorso MS, Lemons RV, Carley TL (2012) Rhyolite-MELTS: A modified calibration of MELTS optimized for silica-rich, fluid-bearing magmatic systems. J Petrol 53:875–890
  11. Hauri E, Wang J, Dixon JE, King PL, Mandeville C, Newman S (2002) SIMS analysis of volatiles in silicate glasses 1. Calibration, matrix effects and comparisons with FTIR. Chem Geol 183:99–114
  12. Hildreth W (1981) Gradients in silicic magma chambers: Implications for lithospheric magmatism. J Geophys R 86:10153–10192
  13. Holloway JR (1981) Volatile interactions in magmas. In Newton RC, Navrotsky A, Woods BJ(eds) Thermodynamics of minerals and melts, Advances in Physical Geochemistry, volume 1, Springer-Verlag, pp 273–293
  14. Imakiire T, Nishimura T (2012) Source model of Kirishima Volcano based on GPS integrated analysis in volcanic region (2nd report). Japan Geoscience Union Meeting 2012 (Abstract), SVC50-P32
  15. Imura R, Kobayashi T (2001) Geological map of volcanoes 11, Kirishima volcano. Geol Surv Japan. (in Japanese with English abstract)
  16. Ishizuka O, Geshi N, Kawanabe Y, Ogitsu I, Taylor RN, Tuzino T, Sakamoto I, Arai K, Nakano S (2014) Long-distance magma transport from arc volcanoes inferred from the submarine eruptive fissures offshore Izu-Oshima volcano, Izu–Bonin arc. J Volcanol Geotherm Res 285:1–17
  17. Japan Meteorological Agency (2013) Development of Quantitative Detection Techniques of Magma Activity and Improvement of Evaluation of Volcanic Activity Level. Technical Reports of The Meteorological Research Institute 69: 152–167. DOI: 10.11483/mritechrepo.69 (in Japanese)
  18. Japan Meteorological Agency (2014a) Volcanic Activity of Kirishimayama Volcano –February – June, 2012 -. Rep Coordinating Comm Prediction Volcan Eruption 112:139–160 (in Japanese)
  19. Japan Meteorological Agency (2014b) Volcanic Activity of Kirishimayama Volcano –June –October, 2012 -. Rep Coordinating Comm Prediction Volcan Eruption 113:148–172 (in Japanese)
  20. Japan Meteorological Agency (2014c) Volcanic Activity of Kirishimayama Volcano –October, 2012 – March, 2013 -. Rep Coordinating Comm Prediction Volcan Eruption 114:174–199 (in Japanese)

21. Japan Meteorological Agency (2014d) Volcanic Activity of Kirishimayama Volcano –February, 2013 –May, 2013 -. Rep Coordinating Comm Prediction Volcan Eruption 115:132–161 (in Japanese)
22. Japan Meteorological Agency (2014e) Volcanic Activity of Kirishimayama Volcano –June, 2013 –October, 2013 -. Rep Coordinating Comm Prediction Volcan Eruption 116:186–208 (in Japanese)
23. Japan Meteorological Agency (2014f) Volcanic Activity of Kirishimayama Volcano –October, 2013 –January, 2014 -. Rep Coordinating Comm Prediction Volcan Eruption 117:186–207 (in Japanese)
24. Japan Meteorological Agency (2016a) Volcanic Activity of Kirishimayama Volcano –February 2014 – May 2014 -. Rep Coordinating Comm Prediction Volcan Eruption 118:124–158 (in Japanese)
25. Japan Meteorological Agency (2016b) Volcanic Activity of Kirishimayama Volcano –May 2014 –October 2014 -. Rep Coordinating Comm Prediction Volcan Eruption 119:213–259 (in Japanese)
26. Japan Meteorological Agency (2018a) Volcanic Activity of Kirishimayama Volcano –February 2015 – May 2015 -. Rep Coordinating Comm Prediction Volcan Eruption 121:259–270 (in Japanese)
27. Japan Meteorological Agency (2018b) Volcanic Activity of Kirishimayama Volcano –June 2015 –October 2015 -. Rep Coordinating Comm Prediction Volcan Eruption 122:347–379 (in Japanese)
28. Japan Meteorological Agency (2018c) Volcanic Activity of Kirishimayama Volcano –October 2015 –January 2016 -. Report of Coordinating Committee for Prediction of Volcanic Eruption 123:293 – 288 (in Japanese)
29. Japan Meteorological Agency (2018d) Volcanic Activity of Kirishimayama Volcano –February 2016 – May 2016 -. Rep Coordinating Comm Prediction Volcan Eruption 124:245–335 (in Japanese)
30. Japan Meteorological Agency (2018e) Volcanic Activity of Kirishimayama Volcano –May 2016 –August 2016 -. Rep Coordinating Comm Prediction Volcan Eruption 125:281–319 (in Japanese)
31. Japan Meteorological Agency (2018f) Volcanic Activity of Shinmoedake in Kirishima. Rep Coordinating Comm Prediction Volcan Eruption 128:225–268 (in Japanese)
32. Japan Meteorological Agency (2018g) Volcanic Activity of Kirishimayama Volcano – September 9, 2017 – January 31, 2018 -. Rep Coordinating Comm Prediction Volcan Eruption 129:249–306 (in Japanese)
33. Japan Meteorological Agency (2018h) Volcanic Activity of Kirishimayama Volcano –February 1, 2018 – May 31, 2018 -. Rep Coordinating Comm Prediction Volcan Eruption 130:213–284 (in Japanese)
34. Japan Meteorological Agency (2019a) Volcanic Activity of Kirishimayama Volcano – September 1, 2017- September 30, 2018 -. Rep Coordinating Comm Prediction Volcan Eruption 131:280–350 (in Japanese)
35. Japan Meteorological Agency (2019b) Volcanic Activity of Kirishimayama Volcano – September 1, 2017- January 31, 2019 -. Rep Coordinating Comm Prediction Volcan Eruption 132:240–311 (in Japanese)
36. Johnson MC, Anderson AT, Rutherford MJ (1994) Pre-eruptive volatile contents of magmas. In: Carroll MR, Holloway JR (eds) Volatiles in magmas, Reviews in Mineralogy, vol 30. Mineralogical

Society of America, Washington DC, pp 281–330

37. Kato K, Yamasato H (2013) The 2011 eruptive activity of Shinmoedake volcano, Kirishimayama, Kyushu, Japan - Overview of activity and Volcanic Alert Level of the Japan Meteorological Agency -. *Earth Planet Space* 65:489–504. 10.5047 /eps.2013.05.009
38. Kawamoto S, Nogami K, Yokokawa M (2011) Crustal deformation associated with the eruption of Shinmoedake volcano, Kirishima volcanic group. *J Geographical Survey Institute* 121:179–182
39. Kilinc A, Carmichael ISE, Rivers ML, Sack RO (1983) The ferric-ferrous ratio of natural silicate liquids equilibrated in air. *Contrib Mineral Petrol* 83:136–140
40. Kita TN, Ikeda Y, Togashi S, Liu Y, Morishita Y, Weisberg MK (2004) Origin of ureilites inferred from a SIMS oxygen isotopic and trace element study of clasts in the Dar al Gani 319 polymict ureilite. *Geochim Cosmochim Acta* 68:4213–4235
41. Kozono T, Ueda H, Ozawa T, Koyagichi T, Fujita E, Tomiya A, Suzuki YJ (2013) Magma discharge variations during the 2011 eruptions of Shinmoe-dake volcano, Japan, revealed by geodetic and satellite observations. *Bull Volcanol* 75:695. doi: 10.1007/s00445-013-0695-4
42. Lowenstern JB (2003) Melt inclusions come of age: volatiles, volcanoes, and Sorby's legacy. In: De Vivo B, Bodnar RJ (eds) *Melt inclusions in volcanic systems, methods, applications and problems*. Elsevier, Amsterdam, pp 1–22
43. Maeno F, Nagai M, Nakada S, Burden RE, Engwell S, Suzuki Y, Kaneko T (2014) Constraining tephra dispersion and deposition from three subplinian explosions in 2011 at Shinmoedake volcano, Kyushu, Japan. *Bull Volcanol* 76:1–16. doi.org/10.1007/s00445-014-0823-9
44. Miyabuchi Y, Hanada D, Niimi H, Kobayashi T (2013) Stratigraphy, grain-size and component characteristics of the 2011 Shinmoedake eruption deposits, Kirishima Volcano, Japan. *J Volcanol Geotherm R* 258:31–46. doi.org/10.1016/j.jvolgeores.2013.03.027
45. Mori T, Kato K (2013) Sulfur dioxide emissions during the 2011 eruption of Shinmoedake volcano, Japan. *Earth Planet Space* 65:573–580. 10.5047 /eps.2013.04.005
46. Nakada S, Nagai M, Kaneko T, Suzuki Y, Maeno F (2013) The outline of the 2011 eruption at Shinmoe-dake (Kirishima), Japan. *Earth Planet Space* 65:475–488. 10.5047 /eps.2013.03.016
47. Nakao S, Morita Y, Yakiwara H, Oikawa J, Ueda H, Takahashi H, Ichianagi M, Ohta Y, Matsushima T, Iguchi M (2013) Volume change of the magma reservoir relating to the 2011 Kirishima Shinmoe-dake eruption – Charging, discharging and recharging process inferred from GPS measurements. *Earth Planet Space* 65:505–515. 10.5047 /eps.2013.05.017
48. Newman S, Lowenstern JB (2002) VolatileCalc: a silicate melt-H<sub>2</sub>O-CO<sub>2</sub> solution model written in Visual Basic for EXCEL. *Comput Geosci* 28:597–604
49. Nishiki K, Oikawa T, Furukawa R, Oishi M, Nakano S, Miyagi I (2013) Amounts of tephra fall deposits from Shinmoedake volcano, during March 2011-February 2012: A preliminary study for immediate estimation of the eruptive mass. *Bull Volcanol Soc Jpn* 58:353–363 (in Japanese with English abstract)

50. Oikawa T, Nagai M, Nakada S, Tajima Y, Miyabuchi Y, Shimano T, Miwa T, Iriyama Y, Ishizuka O, Kawanabe Y, Ito J, Maeno F, Hasenaka T, Kawaguchi M (2018) Amounts of tephra fall deposit from Shinmoedake (Kirishima volcanoes) 2018 eruption (Report 1). In: Abstracts of Volcanol Soc Japan 2018 Fall Meeting (in Japanese), P105, Akita, Japan, 26–30 September 2018
51. Oishi M, Miwa T, Geshi N, Shinohara H, Vinet N (2013) Magma ascent mechanism during the 2011 eruption of Shinmoedake, Kirishima Volcano, Japan, deduced from the analysis of morphology and texture of volcanic ashes. In: Abstracts of Am Geophys Union Fall Meeting, V21B-2712, San Francisco, California, 9–13 December 2013
52. Ohba T, Hitabayashi J, Nogami K, Kusakabe M, Yoshida M (2008) Magma degassing process during the eruption of Mt. Unzen, Japan in 1991 to 1995: Modeling with the chemical composition of volcanic gas. *J Volcanol Geotherm R* 175:120–132. doi: 10.1016/j.jvolgeores.2008.03.040
53. Ohwada M, Kazahaya K, Mori T, Kazahaya R, Hirabayashi J, Miyashita M, Onizawa S, Mori T (2013) Sulfur dioxide emissions related to volcanic activity at Asama volcano, Japan. *Bull Volcanol* 75:775. doi: 10.1007/s00445-013-0775-5
54. Pallister JS, Hoblitt RP, Meeker GP, Knight RJ, Siems DF (1996) Magma mixing at Mount Pinatubo: Petrographic and chemical evidence from the 1991 deposits. In: Newhall CG, Punongbayan RS (eds) *Fire and mud: eruptions and lahars of Mount Pinatubo, Philippines*, Univ Washington Press, pp 687–731
55. Papale P (2005) Determination of total H<sub>2</sub>O and CO<sub>2</sub> budgets in evolving magmas from melt inclusion data. *J Geophys Res* 110:B03208. doi: 10.1029/2004JB003033
56. Putirka KD (2008) Thermometers and barometers for volcanic systems. In: Putirka KD, Tepley FJ III (eds) *Reviews in Mineralogy & Geochemistry*, 69, Minerals, Inclusions and Volcanic processes. Mineralogical Society of America, pp 61–120
57. Saito G, Kazahaya K, Shinohara H, Stimac J, Kawanabe Y (2001) Variation of volatile concentration in a magma system of Satsuma-Iwojima volcano deduced from melt inclusions analyses. *J Volcanol Geotherm R* 108:11–31
58. Saito G, Stimac JA, Kawanabe Y, Goff F (2002) Mafic-felsic interaction at Satsuma-Iwojima volcano, Japan: Evidence from mafic inclusions in rhyolites. *Earth Planet Space* 54:303–325
59. Saito G, Morishita Y, Shinohara H (2010) Magma plumbing system of the 2000 eruption of Miyakejima volcano, Japan, deduced from volatile and major component contents of olivine-hosted melt inclusions. *J Geophys Res* 115:B11202. doi: 10.1029/2010JB007433
60. Saito G, Ishizuka O, Ishizuka Y, Hoshizumi H, Miyagi I (2018) Petrological characteristics and volatile content of magma of the 1979, 1989, and 2014 eruptions of Nakadake, Aso volcano, Japan. *Earth Planet Space* 70:197. <https://doi.org/10.1186/s40623-018-0970-x54:303-325>
61. Saunders K, Blundy J, Dohmen R, Cashman K (2012) Linking petrology and seismology at an active volcano. *Science* 336:1023. doi: 10.1126/science.1220066
62. Shinohara H (2013) Composition of volcanic gases emitted during repeating Vulcanian eruption stage of Shinmoedake, Kirishima volcano, Japan. *Earth Planet Space* 65:667–675. doi:

10.5047/eps.2012.11.001

63. Suzuki Y, Nagai M, Maeno F, Yasuda A, Hokanishi N, Shimano T, Ichihara M, Kaneko T, Nakada S (2013a) Precursory activity and evolution of the 2011 eruption of Shinmoe-dake in Kirishima volcano-insights from ash samples. *Earth Planet Space* 65:591–607. doi: 10.5047/eps.2013.02.004
64. Suzuki Y, Yasuda A, Hokanishi N, Kaneko T, Nakada S, Fujii T (2013b) Syneruptive deep magma transfer and shallow magma remobilization during the 2011 eruption of Shinmoe-dake, Japan- Constraints from melt inclusions and phase equilibria experiments. *J Volcanol Geotherm R* 257:184–204. doi: 10.1016/j.jvolgeores.2013.03.017
65. Tomiya A, Miyagi I, Saito G, Geshi N (2013) Short time scales of magma mixing processes prior to the 2011 eruption of Shinmoedake volcano, Kirishima volcanic group, Japan. *Bull Volcanol* 75:750. doi: 10.1007/s00445-013-0750-1
66. Wallace PJ, Carmichael ISE (1994) S speciation in submarine basaltic glasses as determined by measurements of SKa X-ray wavelength shifts. *Am Mineral* 79:161–167
67. Walker GPL (1989) Gravitational (density) controls on volcanism, magma chambers and intrusions. *Aus J Earth Sci* 36:149–165

## Tables

Tables 1 to 5 are available in the Supplementary Files section

## Figures

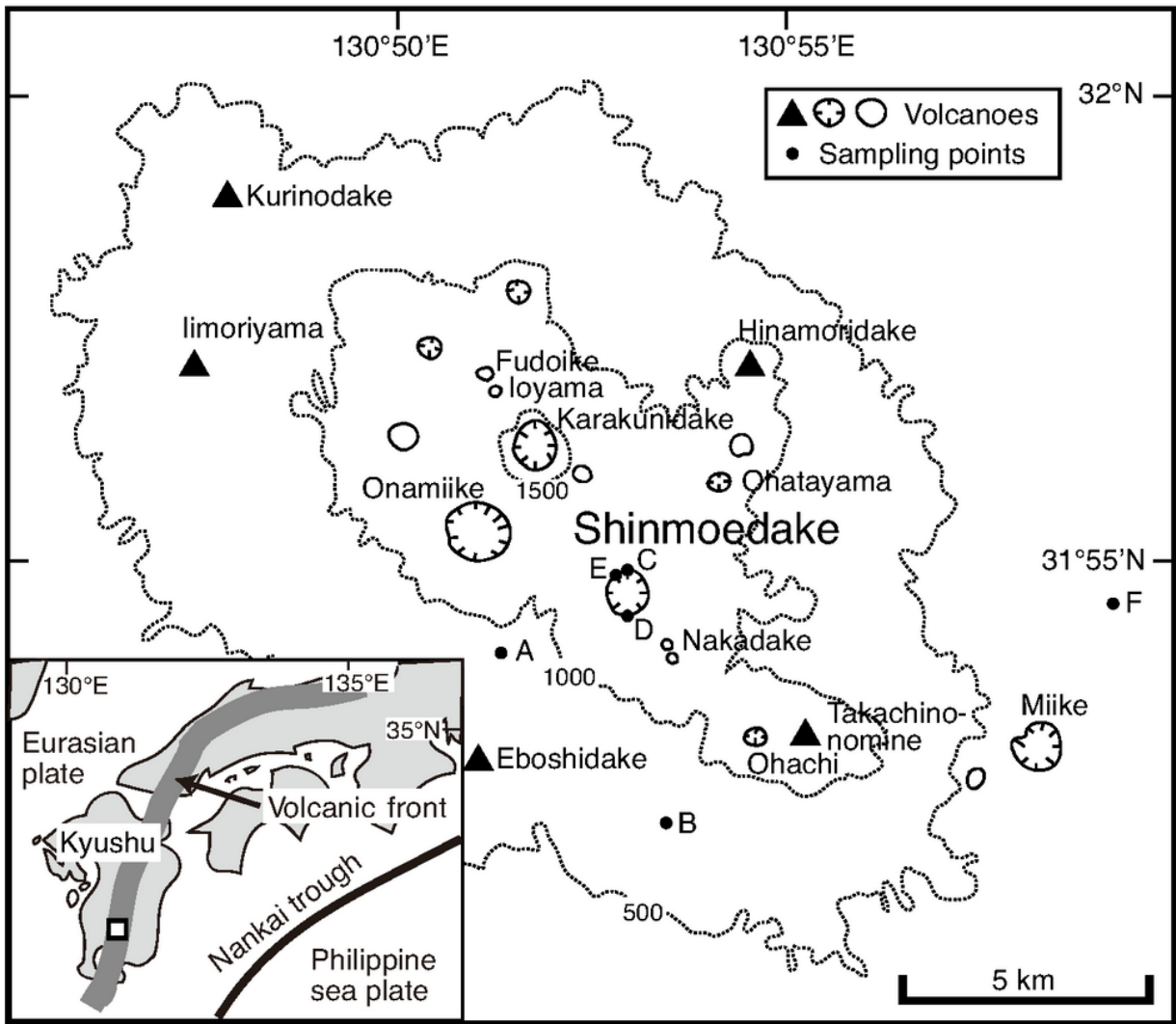


**Figure 1**

Location map showing Shinmoedake, part of the Kirishima volcanic group. Onamiike and Hinamoridake were formed by activity from 100 to 25 ka. Iimoritama, Karakunidake, Shinmoedake, and Takachihonomine were formed by activity from 25 to 0.6 ka. The activity of Shinmoedake began at approximately 18 ka. The Miike maal and Ohachi volcano in the southeastern part of the volcanic group have formed since 0.6 ka, with eruptions occurring at Fudoike, Ioyama, Ohatayama, Nakadake, and Shinmoedake in the center. Ioyama is small lava flow that formed at the northwestern foot of Karakunidake in 1768. Sampling points (A-F) are also shown; A shows the sampling point of 2018-1VGP and 2018-1VS, B shows that of 2018-2VGP and 2018-2VS, C shows that of 2018-3BB1, D shows that of 2018-3BB2 to BB3, E show that of 2018-4L1 to L5 and F shows that of 1235S. Refer to Table 1 for sample names.

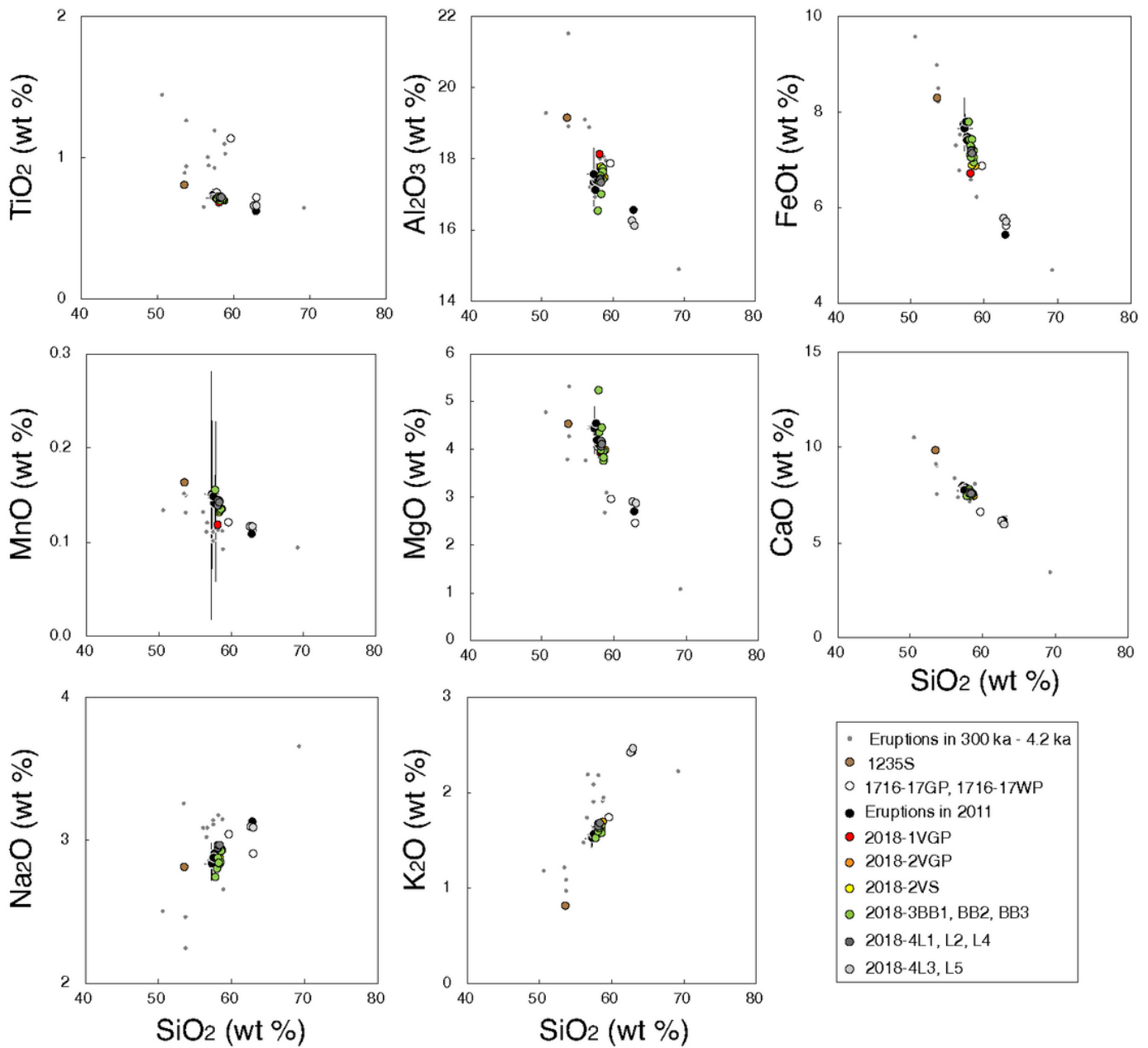


**Figure 2**

Whole-rock chemical compositions of products from the 1235, 1716–17, 2011, and 2018 eruptions (also shown in Table 2). Closed circles denoted “Eruption in 2011” show the chemical compositions of 2011-2SGP, 2011-3SGP, 2011-4VB, 2011-5VL, and 2011-7VL. Red, orange, and yellow circles show the chemical compositions of 2018-1VGP, 2018-2VGP, and 2018-2VS, respectively. Green circles show the chemical compositions of 2018-3BB1 to BB3. Dark gray circles show the chemical compositions of 2018-4L1, L2, and L4. Light gray circles show the chemical compositions of 2018-4L3 and L5. Open, brown, and small gray circles show the whole-rock compositions of 1716-17GP, 1716-17WP, 1235S and previous products

of the younger Kirishima volcanoes (300 ka–4.2 ka), respectively. Error bars show standard deviations for each analysis (Tomiya et al. 2013) shown in Table 2. Refer to Table 1 for sample names.

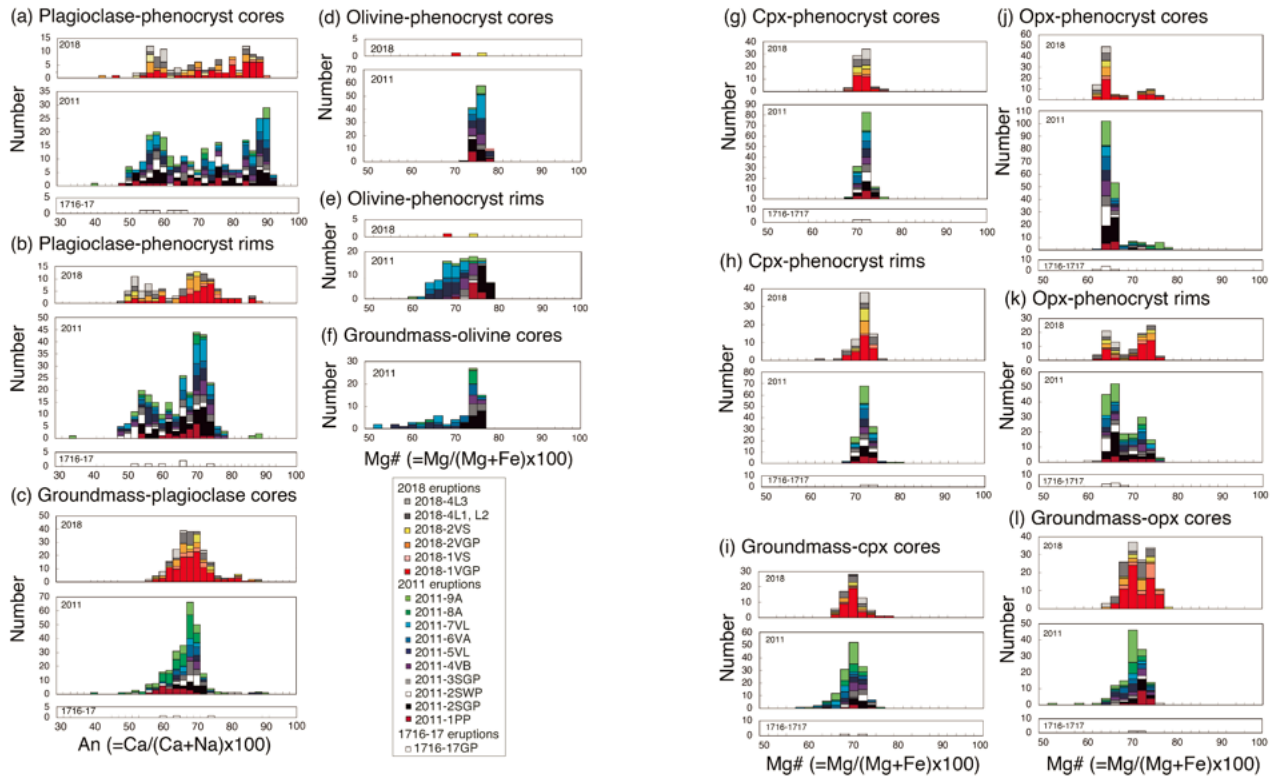


**Figure 3**

Chemical compositions of (a) plagioclase-phenocryst cores, (b) plagioclase-phenocryst rims, (c) groundmass-plagioclase cores, (d) olivine-phenocryst cores, (e) olivine-phenocryst rims, (f) groundmass-olivine cores, (g) clinopyroxene-phenocryst cores, (h) clinopyroxene-phenocryst rims, (i) groundmass-clinopyroxene cores, (j) orthopyroxene-phenocryst cores, (k) orthopyroxene-phenocryst rims, and (l) groundmass-orthopyroxene cores.  $An = Ca/(Ca+Na) \times 100$  % in mol.  $Mg\# = Mg/(Mg+Fe) \times 100$  % in mol. Refer to Table 1 for sample names. Plagioclase-phenocryst cores in the 2011 and 2018 products show  $An_{42-94}$  and  $An_{44-91}$ , respectively, while the plagioclase-phenocryst rims in the 2011 and 2018 products showing  $An_{34-90}$  and  $An_{50-90}$ , and groundmass-plagioclase cores in the 2011 and 2018 products showing  $An_{40-90}$  and  $An_{57-88}$ , respectively. The olivine phenocrysts from the 2011 products have  $Fo_{74-80}$  cores and  $Fo_{60-76}$  rims. Groundmass-olivine cores in the 2011 products have  $Fo_{52-78}$ . The 2018 products have rare olivine phenocrysts and no groundmass-olivines. Clinopyroxene-phenocrysts cores of the 2011 and 2018 products show  $Wo_{34-45}En_{40-47}Fs_{13-20}$  and  $Mg\#70-77$  and  $Wo_{39-46}En_{38-45}Fs_{14-18}$  and  $Mg\#69-76$ , respectively. Clinopyroxene-phenocrysts rims of the 2011 and 2018 products show  $Wo_{33-45}En_{40-50}Fs_{13-19}$  and  $Mg\#70-80$  and  $Wo_{38-46}En_{37-46}Fs_{14-18}$  and  $Mg\#68-76$ , respectively. Groundmass-clinopyroxene

cores of the 2011 and 2018 products show  $Wo_{15-44}En_{34-62}Fs_{13-36}$  and  $Mg\#60-76$  and  $Wo_{12-43}En_{40-64}Fs_{12-28}$  and  $Mg\#67-79$ , respectively. Orthopyroxene-phenocryst cores of the 2011 and 2018 products show  $Wo_{1-6}En_{61-77}Fs_{21-36}$  and  $Mg\#63-79$  and  $Wo_{2-4}En_{61-75}Fs_{22-37}$  and  $Mg\#62-77$ , respectively. Orthopyroxene-phenocryst rims of the 2011 and 2018 products show  $Wo_{2-5}En_{62-74}Fs_{23-38}$  and  $Mg\#62-76$  and  $Wo_{2-5}En_{61-74}Fs_{23-36}$  and  $Mg\#63-77$ , respectively. Groundmass-orthopyroxene cores of the 2011 and 2018 products show  $Wo_{2-11}En_{57-74}Fs_{22-35}$  and  $Mg\#60-76$  and  $Wo_{2-8}En_{63-76}Fs_{20-34}$  and  $Mg\#65-79$ , respectively.

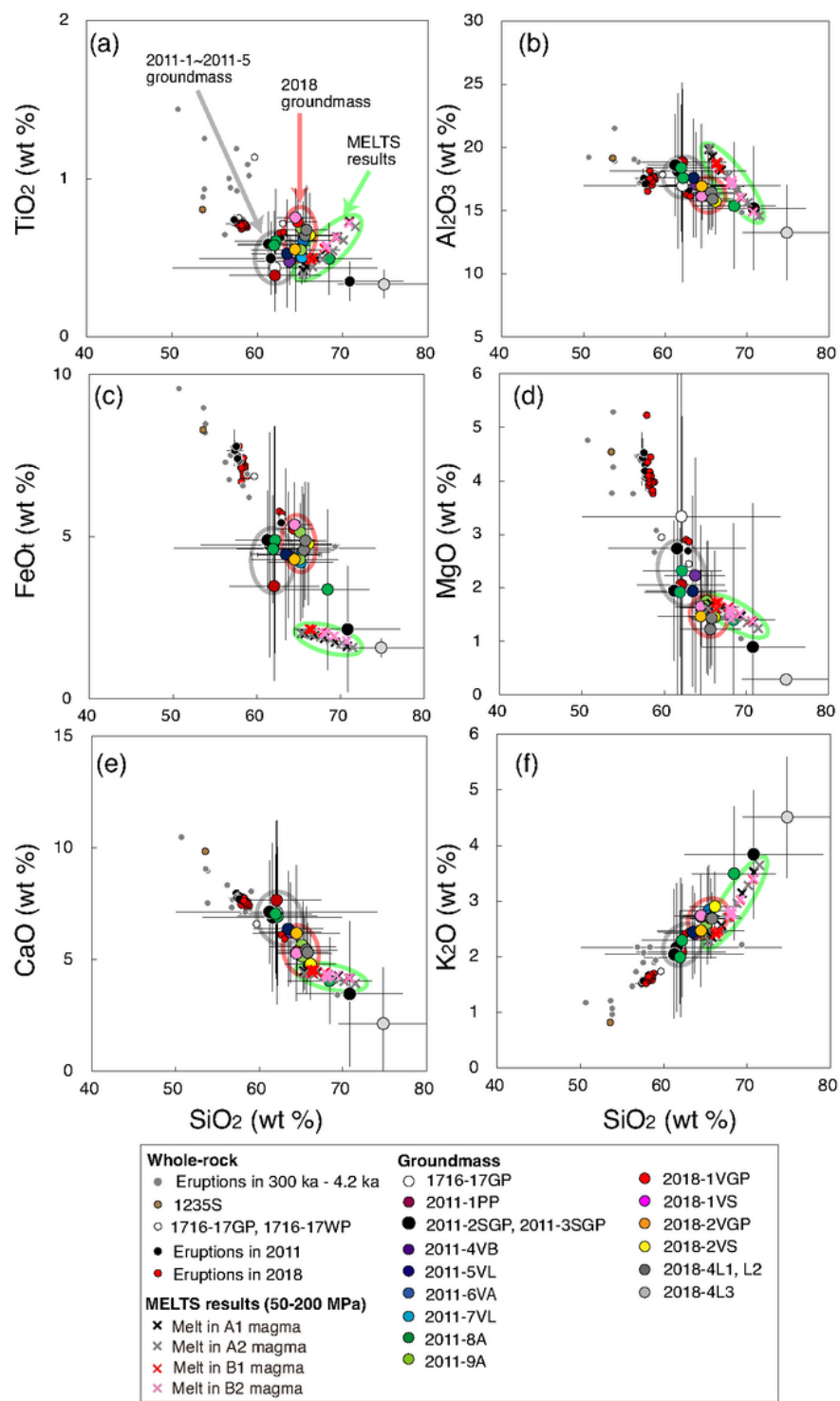


**Figure 4**

Chemical compositions of groundmass in products from the 2011 and 2018 eruptions. (a) TiO<sub>2</sub>- versus SiO<sub>2</sub> contents; (b) Al<sub>2</sub>O<sub>3</sub>- versus SiO<sub>2</sub> contents; (c) FeOt- versus SiO<sub>2</sub> contents; (d) MgO- versus SiO<sub>2</sub> contents; (e) CaO- versus SiO<sub>2</sub> contents; and (f) K<sub>2</sub>O- versus SiO<sub>2</sub> contents. Large circles and error bars show the groundmass compositions of products and their standard deviations, respectively (also shown in Additional file 3). Chemical compositions of melts at pressures of 50–200 MPa calculated with the

MELTS program (Gualda et al. 2012) (Additional file 8) are also shown. Whole-rock chemical compositions of the products from the 2011 and 2018 eruptions and previous eruptions are shown using the same symbols in Figure 2. The small open and closed circles show whole-rock compositions for the 1716–17 eruptions and previous products from the younger Kirishima volcanoes (300 ka – 4.2 ka), respectively.

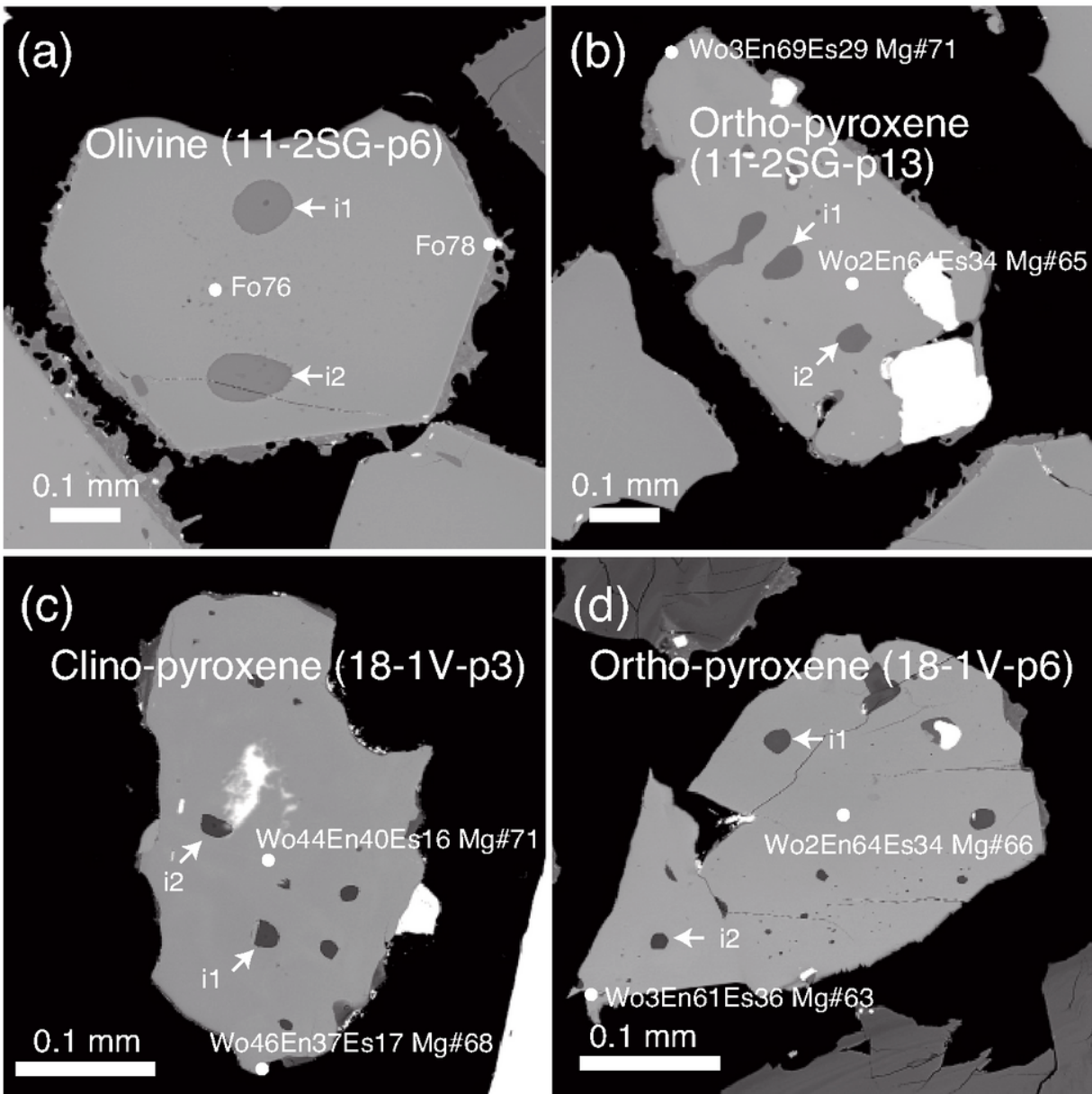
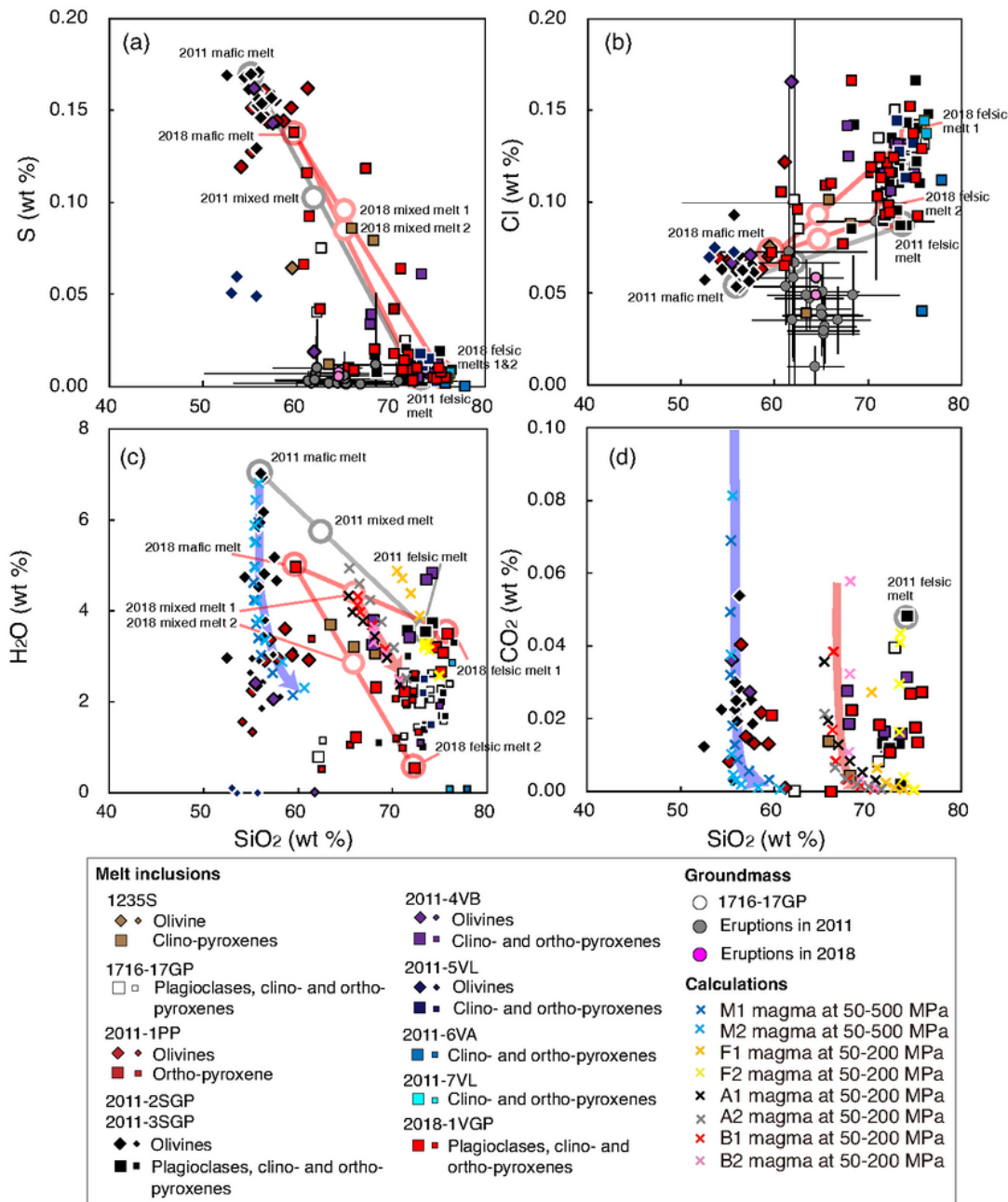


Figure 5



## Figure 6

Chemical compositions of melt inclusions in products from the 2011 and 2018 eruptions. (a)  $\text{Al}_2\text{O}_3$ - versus  $\text{SiO}_2$  contents; (b)  $\text{MgO}$ - versus  $\text{SiO}_2$  contents; (c)  $\text{CaO}$ - versus  $\text{SiO}_2$  contents; and (d)  $\text{K}_2\text{O}$ - versus  $\text{SiO}_2$  contents. Large circles with error bars indicate chemical compositions of the groundmasses and the standard deviations, respectively (also shown in Figure 4). Chemical compositions of groundmasses from the 2011 eruptions (2011-1PP, 2011-2SGP, 2011-2SWP, 2011-3SGP, 2011-4VB, 2011-5VL, 2011-6VA, 2011-7VL, 2011-8A, and 2011-9A) are denoted by gray circles. Chemical compositions of groundmasses from the 2018 eruptions (2018-1VGP, 2018-1VS, 2018-2VGP, 2018-2VS, and 2018-4L1 to L3) are represented by light red circles. Chemical composition of groundmasses in the form of gray pumices from 1716–17 are open circles. Whole-rock chemical compositions of products from the 2011 and 2018 eruptions and previous eruptions are shown using the same symbols as in Figure 2. Chemical compositions of melts (M1 and M2 magmas at pressure ranges of 50–500 MPa and F1, F2, A1, A2, B1, and B2 magmas at pressure ranges of 50–200 MPa) calculated using the MELTS program (Additional file 8) are also shown.



**Figure 7**

Volatile and  $\text{SiO}_2$  contents in melt inclusions and groundmasses: (a) Sulfur- versus  $\text{SiO}_2$  contents; (b) Cl- versus  $\text{SiO}_2$  contents; (c)  $\text{H}_2\text{O}$ - versus  $\text{SiO}_2$  contents; and (d)  $\text{CO}_2$ - versus  $\text{SiO}_2$  contents.  $\text{H}_2\text{O}$  and  $\text{CO}_2$  contents of the melt inclusions were measured by SIMS and the S and Cl contents by EPMA, except for the small symbols in (c), which indicate that the  $\text{H}_2\text{O}$  content was measured by EPMA (shown in

Additional file 4). Analytical errors for H<sub>2</sub>O and CO<sub>2</sub> by SIMS are ±0.2 wt % and ±0.0028 wt % (Saito et al. 2010). Analytical errors for H<sub>2</sub>O, S, and Cl by EPMA are ±1 wt %, ±0.007 wt%, and ±0.004 wt %, respectively (Saito et al. 2018). H<sub>2</sub>O, CO<sub>2</sub>, and SiO<sub>2</sub> contents of melts (M1 and M2 magmas at pressure ranges of 50–500 MPa and F1, F2, A1, A2, B1, and B2 magmas at pressure ranges of 50–200 MPa) calculated using the MELTS program (Additional file 8) are also shown. Gray lines with circles indicate mixing of mafic and felsic melts in the 2011 magma (Table 4). Red lines with circles indicate mixing of mafic and felsic melts in the 2018 magma (Table 4). Blue and red curves with arrows show the compositional changes in melts that are expected from a decrease in the pressures of the 2011 mafic magma and 2018 magma, respectively.

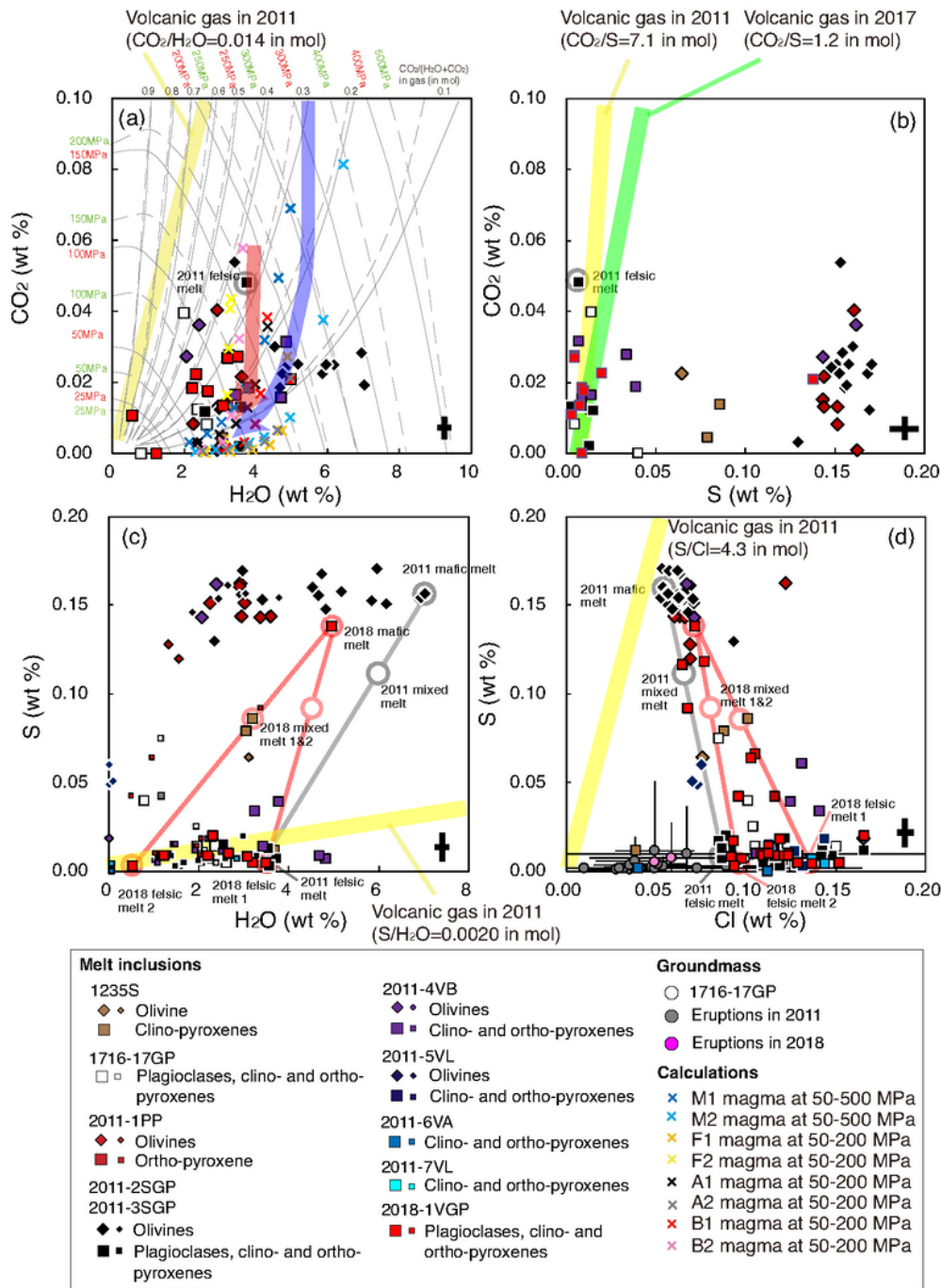
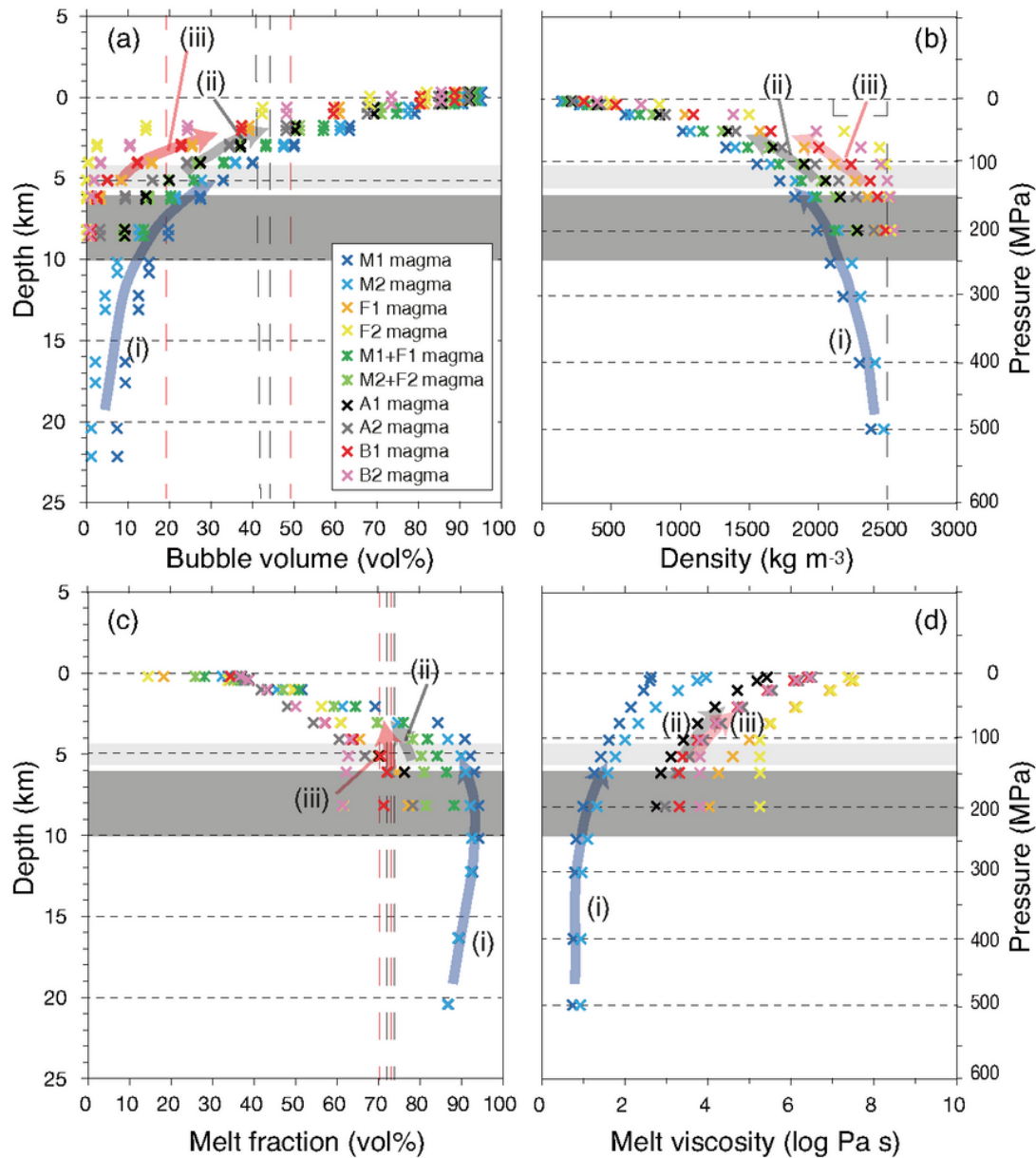


Figure 8

Volatile content of melt inclusions and groundmasses: (a)  $\text{H}_2\text{O}$  - versus  $\text{CO}_2$  contents, (b)  $\text{H}_2\text{O}$ - versus S contents, (c)  $\text{CO}_2$ - versus S contents, and (d) S- versus Cl contents. Error bars indicate analytical errors for  $\text{H}_2\text{O}$  and  $\text{CO}_2$  by SIMS and S and Cl by EPMA. The analytical errors in  $\text{H}_2\text{O}$  by EPMA in (c) are  $\pm 1$  wt % (Saito et al. 2018).  $\text{H}_2\text{O}$  and  $\text{CO}_2$  contents in melts (M1 and M2 magmas at pressure ranges of 50–500

MPa and F1, F2, A1, A2, B1, and B2 magmas at pressure ranges of 50–200 MPa) calculated using the MELTS program (Additional file 8) are also shown. Solid and broken curves in (a) indicate solubilities of the H<sub>2</sub>O-CO<sub>2</sub> gas mixture in the 2011 mafic melt (Table 4) at 1030 °C and the 2011 felsic melt (Table 4) at 870 °C, respectively, calculated using the solubility model of Ghiorso and Gualda (2015). Gray lines with circles in (c) and (d) indicate mixing of mafic and felsic melts in the 2011 magma (Table 4). Red lines with circles in (c) and (d) indicate mixing of mafic and felsic melts in the 2018 magma (Table 4). Blue and red curves with arrows in (a) show expected compositional changes in the melts resulting from a decrease in the pressure of the 2011 mafic magma and 2018 magma, respectively. Yellow lines show CO<sub>2</sub>/H<sub>2</sub>O, CO<sub>2</sub>/S, S/H<sub>2</sub>O, and H<sub>2</sub>O/S ratios of the volcanic gases observed in 2011 (Shinohara 2013; Additional file 10). Green line in (b) shows CO<sub>2</sub>/S ratios of the volcanic gas observed in 2017 (GSJ 2017; Additional file 10). The same symbols are used as in Figure 7.



**Figure 9**

Physical properties of magmas associated with the 2011 and 2018 eruptions at a pressure range of 5 to 500 MPa calculated from bulk volatile content (Table 4) using MELTS calculation and the molar volume of the H<sub>2</sub>O and CO<sub>2</sub> gases (Additional file 7): (a) Bubble volume of magmas (vol%), (b) Density of magmas (kg m<sup>-3</sup>), (c) Melt fraction of magmas (vol%), and (d) Melt viscosity of magmas (log Pa s). Further data is given in Additional files 8 and 9. Dark gray areas in (a) to (d) indicate depth of crustal deformation estimated by geophysical observation during 2009–2018 (6–10 km; GIAJ 2012; Ueda et al. 2013; Nakao et al. 2013; JMA 2019b). Light gray areas in (a) to (d) indicate depth of the silicic andesite magma chamber estimated by petrological study of the 2011 products (105–135 MPa; Suzuki et al.

2013b). Black broken lines in (a) indicate maximum and minimum porosities of the subplinian eruption products from 2011 (42–45 vol% for 2011-2SGP and 2011-3SGP; Additional file 1). The same bubble volumes are reproduced in the M1+F1 to M2+F2 magmas at pressure ranges of 50–75 MPa. Red broken lines in (a) indicate maximum and minimum porosities of the vulcanian eruption products in 2018 (19–49 vol% for 2018-1VGP, 2018-1VS, 2018-2VGP, and 2018-2VS; Additional file 1). The same bubble volumes were reproduced in B1 and B2 magmas at pressure ranges of 25–100 MPa. Broken lines in (b) indicate expected density structure of the crust based on a study by JMA (2013) that reports densities of 2000–2500 kg m<sup>-3</sup> at depths of less than 0 km bsl and approximately 2500 kg m<sup>-3</sup> at depths of 0–1 km bsl based on analyses of borehole samples around the Kirishima volcanoes. We assumed a density structure of 2000–2500 kg m<sup>-3</sup> at a depth of 0–1 km and 2500 kg m<sup>-3</sup> at depths of more than 1 km beneath Shinmoedake by considering the height of the Shinmoedake summit crater above sea level prior to the 2011 eruptions (1.2 km). Black broken lines in (c) indicate maximum and minimum groundmass content of the subplinian eruption products in 2011 (72–74 vol% for 2011-2SGP and 2011-3SGP). The same melt contents are reproduced in the M1+F1 and M2+F2 magmas at pressure ranges of 50–100 MPa. Red broken lines in (c) indicate maximum and minimum groundmass content in the vulcanian eruption products from 2018 (70–73 vol% for 2018-1VGP, 2018-1VS, 2018-2VGP, and 2018-2VS; Additional file 1). The same melt content was reproduced in the B1 magma at pressure ranges of 125–300 MPa; however this melt content was not obtained for the B2 magma at pressure ranges of 5–500 MPa, which suggests that the B1 magma with an H<sub>2</sub>O content of 3.0 wt% might be more realistic for 2018 than the B2 magma. Blue curves with arrows (i) show expected physical property changes in the 2011 mafic magma during its ascent. Gray curves with arrows (ii) and red curves with arrows (iii) show expected physical property changes in the 2011 and 2018 magmas during their ascent, respectively.

## Supplementary Files

This is a list of supplementary files associated with this preprint. Click to download.

- [krsmimanutables220314.pdf](#)
- [krsmimanuadditional220314.docx](#)
- [krsmimanugraphicalabstfig220314.png](#)